https://dx.doi.org/10.1016/j.cej.2021.132144

Reconstruction and optimization of LSCF cathode microstructure based on Kinetic Monte Carlo method and Lattice Boltzmann method

Chengru Wu[a,b], Yang Wang[a,b], Yuze Hou[a], Xing Li[a], Zhijun Peng[a] , Qing Du[a*], Meng Ni[b*], Kui Jiao[a*]

[a]State Key Laboratory of Engines, Tianjin University

135 Yaguan Road, Tianjin, China, 300350

[b]Building Energy Research Group, Department of Building and Real Estate

The Hong Kong Polytechnic University, Hung Hom, Kowloon, Hong Kong, China

*Corresponding authors: kjiao@tju.edu.cn (K. Jiao); duqing@tju.edu.cn (Q. Du); meng.ni@polyu.edu.hk (M. Ni)

Tel: +86-22-27404460; fax: +86-22-27383362

Highlights:

- A Kinetic Monte Carlo Model is established for quick reconstruction.
- An LBM method is conducted for performance evaluation of reconstructed electrodes.
- Local O2 partial pressure plays decisive role in the ohmic loss at $p_{\mathrm{O_2}} < 0.1$ bar .
- Enhancement of electrode connectivity rather than porosity dominant ohmic loss.
- The infiltrated electrodes promote performance and reaction uniformity.

Abstract

Solid phase sintering is a critical process for fabricating mixed ionic and electronic conductivity (MIEC) electrodes. In this study, the microstructures of MIEC electrodes are numerically reconstructed by a Kinetic Monte Carlo method. The performance of the reconstructed

MIEC electrodes is then evaluated by a pore scale Lattice Boltzmann model. The present study provides the first comprehensive assessment of local O_2 partial pressure on electrode performance. It is found that ohmic loss tends to play remarkable roles at a low O_2 partial pressure of $p_{O_2} < 0.1\ \text{bar}$. As insufficiency of O_2 is almost unavoidable in the SOFC stack, the influence of local O_2 partial pressure on ionic conductivity should be considered in LSCF modeling. Another important finding is that the initial states of compact powder have a profound impact on the electrode performance. Small initial grain size and irregular particles both contribute to generate large reaction area after sintering thereby decrease activation loss. It is also found that compact powder consistency even plays a more important role in electrode performance than particle size. The study also provides deep insight into influence of sintering process. The effective conductivity of electrode is mainly controlled by the enhancement of electrode connectivity. Subsequently, nanostructured SOFC electrodes by infiltration/impregnation are reconstructed evaluated numerically. The infiltrated electrodes demonstrate improved performance and significantly promote uniformity of reaction rates. The present study forms a solid foundation for optimization of the fabrication procedures to improve the fuel cell performance.

Graphical abstract

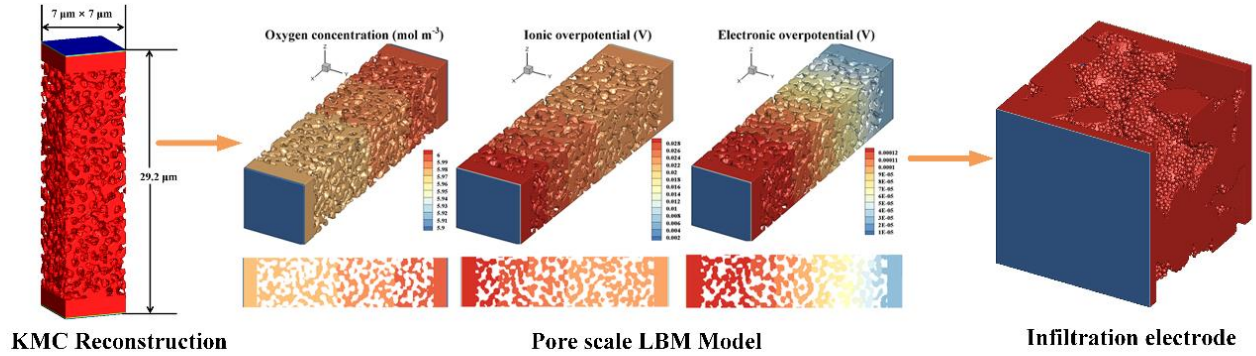

Key word: MIEC; Kinetic Monte Carlo; Lattice Boltzmann model; Microstructure reconstruction; Infiltrated electrode; Solid oxide fuel cell.

Nomenclature

A	Area (m^2)
C	Concentration (mol m^{-3})
D	Diffusion coefficient (m^2 s^{-1})
e	Discrete velocities
E	Free energy (J)
f	Distribution function
F	Faraday’s constant (C mol^{-1})
I	Current density (A m^{-2})
j	Exchange current density (A m^{-3})
J	Electrochemical reaction rates (A m^{-3})
J	Interaction energy (J)
k	Pre-exponential factor
K_B	Boltzmann’s constant
m	Transformed distribution function
M	Molecular weight (kg mol^{-1})
M	Transformation matrix
n	Total number of neighboring pixels
N	Total number of pixels
p	Partial pressure (Pa)
P	Operation pressure (Pa)
P	probability
q	Pixel value

R	Universal gas constant (J mol^{-1} K^{-1})
r	Radius (μm)
S	Source term
t	Time (s)
T	Temperature (K)
V	Mole volume (m^{3} mol^{-1})
Greek	
α	Transfer coefficient
ρ	Density (kg m^{-3})
δ	Kronecker delta function
ξ	Tortuosity
ζ	Arithmetic mean value
ε	Porosity
φ	Potential (V)
β	Transfer coefficient
w	Weight coefficient
λ	Weighting factor
ψ	Relative volume fraction
η	Overpotential (V)
Ω_D	Collision integral
κ	Conductivity (S m^{-1})
γ	Reaction order
τ	Relaxation coefficient

Subscripts and superscripts

act	Activation
ave	Average
eff	Effective
ele	Electronic
eq	Equilibrium
ion	Ionic
NS	Surface area of nanoparticles
TS	Total surface area
0	Standard state

1. Introduction

In recent decades, development of intermediate temperature Solid Oxide Fuel Cell (IT-SOFC) has become promising strategy to reduce the cost and improve the durability of SOFC system [1]. Mixed ionic and electronic conductors (MIECs) such as $La_{0.6}Sr_{0.4}Co_{0.2}Fe_{0.8}O_3$ (LSCF) perovskite are promising cathode materials for IT-SOFC. These MIECs show good ionic and electronic conductivities and excellent electrocatalytic activity towards oxygen reduction reaction (ORR) at a temperature range of 600-800 ℃ [2], [3]. Unlike traditional composite electrodes where the electrochemical reactions occur at the triple phase boundary (TPB) [4], [5], electrochemical reaction of MIEC electrode can occur on the entire surface of MIEC particles [6], [7], which is effective in reducing the electrode activation loss under intermediate temperature conditions [8]. As the porous microstructure provides paths for gas and charge transport as well as sites for electrochemical reactions, it is of great importance to gain a fundamental understanding on how the electrode microstructure affect the transport of ions/electrons/gas species and the electrochemical reaction processes. Electrode microstructure reconstruction is thus critical for understanding the electrode microstructure properties and for electrode design optimization.

The electrode microstructure can be reconstructed both experimentally and numerically. In recent years, the focused ion beam scanning electron microscope (FIB-SEM) tomography or X-ray computed tomography (XCT) have demonstrated their capability for electrode microstructure reconstruction and analysis [9], [10]. However, FIB-SEM or XCT method are time-consuming and expensive [11]. It is also difficult to generalize the findings and conclusions based on limited experimental samples. For comparison, the electrode microstructure can be reconstructed numerically in an efficient and cost-effective manner by numerical sintering approaches including Kinetic Monte Carlo (KMC) method and Phase Field method (PFM) [12], [13]. Both methods simulate the sintering process by the principle of reducing the total free energy of the system. PFM solves partial differential equations to describe interface status to obtain the evolution of the phase field with comprehensive consideration of various factors of sintering [14]. However, this method is also time consuming and needs large computing resources. It can be used to study electrode degradation process but is not very suitable if quick reconstruction of electrode microstructure is needed [15]. Compared with PFM, the KMC makes a series of simplification for sintering kinetics to significantly improve the computational efficiency with reasonable accuracy in microstructure reconstruction [16].

As SOFC works at high temperatures (600 - 1000 ℃), it is very challenging to experimentally reveal the complex in-situ electrochemical process inside the electrode [17]-[19]. For comparison, numerical modeling is capable of capturing the electrochemical and species transport characteristics inside the porous electrodes [20]. Due to the importance of MIEC electrodes and the complicated processes involved in MIEC, electrochemical reaction mechanism inside the

MIEC has been the subject of many modeling studies. Most of previous model studies on LSCF adopt the homogeneous hypothesis while the influences of real structure are neglected. Francesco Ciucci et al. developed a 2D numerical model to investigate the surface reaction and transport properties of MIEC electrode. They found that surface reaction rather than electron migration is the overall rate-limiting step [21]. Fleig J and J. Maier developed a 3D numerical model to describe species, ion, and electron transport at electrochemically active sites [22]. It was found that appropriate combinations of ionic conductivity and surface reaction coefficient are necessary to achieve acceptable polarization resistances. Gong et al. built a modified one-dimensional continuum model to analyze the oxygen reduction on LSM-type MIEC composite [23] cathode by incorporating multi-step charge-transfer into the bi-pathway kinetics. Although extensive research works have been carried out on MIEC cathode, only a few studies take real structure of electrode into account. K. Matsuzaki et al. developed a 3D pore scale model based on Lattice Boltzmann method to investigate the chemical potential and current vector distributions inside LSCF [24]. FIB-SEM method was introduced to qualify micro-characteristics in their study. So far, very little attention has been paid to the role of sintering process on MIEC electrode performance. Moreover, kinetic sintering is beneficial for electrode conductivity and structural strength while densification of the particles reduces the effective reaction area. In addition, experimental research shows that nanostructured electrodes by infiltration/impregnation can significantly improve the electrochemical reaction sites, leading to enhanced electrode performance [25], [26]. Zhang et al. developed a numerical infiltration/impregnation method to evaluate effects of infiltration process on microstructure properties. However, the electrochemical performance of the infiltrated electrodes has not been comprehensively studied yet. Actually, the understanding about infiltrated electrode microstructure and its impact mechanism on SOFC performance are still limited [27].

Recently, the mesoscopic Lattice Boltzmann method has raised more concern and becoming a promising tool for real microstructure simulation owing to its excellent parallelism and complex boundary processing capabilities [28]-[30]. Researchers' efforts have devoted to the application of Lattice Boltzmann method to analyze the transport process inside real microstructure geometries. Aidun et al. comprehensively summarized the applications of LBM in complex and multiscale flows and it was emphasized that LB method would be one of the valuable candidates for fluid dynamics [31]. Li et al. proposed a three dimensional two-fluid-phase LB model to investigate the viscous coupling effects inside porous media [32]. Patel et al. proposed an LBM based reactive transport model to simulate microstructure evolution of ordinary Portland cement paste. It was found that leaching rate is directly proportional to the ability of calcium transportation [33]. Lee et al. developed an LBM based two-dimensional multi-phase fluid mixture model to observe the electrolyte microscopic behavior inside the porous media of lithium-ion batteries (LIBs) [34]. Taken together, Lattice Boltzmann method provides an efficient approach for the solution of flow problems that is also particularly desirable for the investigation of coupled mass and charge transport process inside porous media.

In the present paper, a Kinetic Monte Carlo method is established to generate real microstructure for LSCF electrode. Unlike the previous studies on LSCF, the sintering kinetics of LSCF materials are considered during reconstruction process in the present study. The electrochemical performance of the generated LSCF electrodes is then evaluated numerically to understand how the sintering processes and sintering conditions affect the LSCF electrode performance, which has not been reported yet. Lattice Boltzmann method is conducted to solve the diffusion equations to describe the coupled transport and electrochemical reactions. Species, polarization loss and reaction rates distribution inside real electrode are comprehensively investigated. Influence of oxygen partial pressure and sintering process such as initial particle size and initial particle shape on electrode performance are comprehensively analyzed. The aim of the above parametric studies is to gain a fundamental understanding on how the sintering fabrication conditions affect the electrode performance so as to optimize the fabrication procedure for performance enhancement. The nanostructure electrodes by infiltrated are also studied.

2. LSCF electrode microstructure reconstruction by Kinetic Monte Carlo Method

Kinetic Monte Carlo method is employed in the present study to generate the real microstructure of LSCF electrode. Compared with other approaches, the KMC method takes sintering kinetic of MIEC electrode into consideration to ensure reasonable accuracy with good computational efficiency. Another advantage of KMC simulation is that it allows the control of sintering process. Therefore, it becomes much more convenient to generate specific electrode microstructures by controlling the sintering conditions. In simple terms, the KMC sintering is dependent on the calculation of total free energy whereby all the nearest (common side) and next-nearest neighbors (common corner) contribute specific units of interaction energy to the computational system:

$$E = \frac{1}{2}\sum_{i}^{N}\sum_{j}^{n} J\left(q_i, q_j\right) w_{i,j}\left[1-\delta\left(q_i, q_j\right)\right] \tag{1}$$

where E represents total free energy of the system. i represents number of pixels. N is total number of pixels. q represents pixel value of different particles. j is the neighbor pixel number. n represents total number of neighbor pixels. The two values of $w_{i,j}$ are conducted to distinguish the contribution of different adjacent pixels (nearest and next-nearest neighbors) to the free energy of the system [35]. For nearest neighbors, $w_{i,j}$ is taken to be 1 since surface energy is defined based on surface contact of common side. For next-nearest neighbors, $w_{i,j}$ varies over the range 0 to 1 to describe the weakened surface energy. The value of $w_{i,j}$ is chose to be $1/\sqrt{2}$ in this study [35]. This is equivalent to assuming that the interaction energy is inversely proportional to their distance from the center pixel. J is the surface energy of pixel i and pixel j which is dependent on the properties of materials with a range of 0.5-2 J m^{-1}. Only interactions between different particles or between particles and pores have impacts on system free energy. A Kronecker delta function is carried out here to judge this kind of relationship:

$$\delta = \begin{cases} 1 & q_i \neq q_j \\ 0 & q_i = q_j \end{cases} \tag{2}$$

It is hypothesized that free energy reduction is achieved by three ways during KMC process: (1) grain growth, (2) pore migration, and (3) vacancy formation and annihilation.

Grain growth

Grain growth is simulated by exchanging a randomly selected grain pixel with an arbitrary neighboring grain site. Firstly, it is assumed that the exchange has already occurred. The system free energy change caused by the exchange is calculated by:

$$\Delta E = E_{\text{initial}} - E_{\text{final}} \tag{3}$$

Where E_{initial} means the initial system free energy while E_{final} is the system free energy after exchanging. Then a standard Metropolis method is conducted to proceed the probability P based on the virtual exchange process, which is calculated by:

$$P = \begin{cases} 1 & \Delta \mathrm{E}<0 \\ e^{\left(-\frac{\Delta \mathrm{E}}{K_B T}\right)} & \Delta \mathrm{E}>=0 \end{cases} \tag{4}$$

Where K_{B} is the Boltzmann's constant and T is the temperature. Instead of using absolute temperature for simulation, normalized $K_{\mathrm{B}}T$ is employed to represent the dimensionless temperature in KMC study. Whether the exchange accepted or not is dependent on the comparison of above probability with the specific grain growth frequency. If the value of P larger than the grain growth frequency, the exchange is accepted. Otherwise, the system is restored to its original state.

Pore migration

Pore migration is reached by exchanging a pore pixel at random with a neighboring grain site. Standard Metropolis method is also used here to obtain the specific probability to realize the acceptance of the exchanging attempt.

Vacancy formation and annihilation

It should be noticed that pore and vacancy are different concept. A pore is defined as ensembles of contiguous pore sites and a vacancy means a single pore site isolated from grain sites, which is harmful for connectedness of electrode. Therefore, we can reasonably assume that that once vacancies are formed, it will be annihilated in the next KMC step with a small vacancy annihilation frequency. Vacancy annihilation is thought to occur along the thickness of sintering system in this study, which is also consistent with the experimental results [35].

Both the grain growth and pore migration process contribute to the growth of sintering necks while vacancy formation and annihilation promote the electrode densification. The operation of KMC method is based on the interface recognition to realize the efficient and accurate pixel exchange. Firstly, the initial compact powders are randomly generated by a morphological dilation method inside an empty 3D domain [36]. The 3D domain is discrete into pixel voxels. The specific value of pixel is defined to represent different particles or pore phases. There are two kinds of grain and surface boundaries existed in a MIEC electrode where MIEC-MIEC and MIEC-pore contact with each other. Secondly, the grain and surface boundaries are explicitly identified to further judge the exchange mode for system free energy reduction. Then, all of the surface boundary pixels and grain boundary pixels are randomly selected to execute the grain growth or pore migration steps. Importantly, each surface or grain boundary pixels have an opportunity to exchange during one KMC step. Finally, vacancy formation and annihilation step are employed to ensure the stability and reliable of reconstructed porous media. The real sintering time is proportional to the simulation steps in accordance with previous studies [9]-[12]. The similarity of appearance with experimental samples is not enough to prove the reliability of numerical sintering reconstruction. Evolution of critical micro-properties including relative density and surface area during different sintering stages should be comprehensively evaluated and compared with experimental results to further reveal the reliability of reconstruction process [12]. The necessary kinetic parameters used for KMC simulation are exhaustively provided in Table 1 below.

Number	Model input parameters	Value
1	Initial particle size	0.4 μm
5	Grain growth frequency	0.4
6	Pore migration frequency	0.3
7	Vacancy annihilation frequency	0.005
8	Dimensionless temperature	2.3
9	Surface energy of LSCF	1.5 J

Table 1 Design of kinetic parameter for KMC simulation

3. Performance evaluation of the reconstructed LSCF electrodes

3.1 Species transportation

In pore phases, the oxygen diffusion is governed by concentration gradient while convection effect is neglected duo to low gas flow velocity. The governing equation is shown as:

$$\nabla \cdot \left(D_{\mathrm{O_2}}^{\mathrm{eff}} \nabla C \right) = S \tag{5}$$

Where C (mol m^3) is oxygen concentration inside electrodes. S means oxygen reduction reaction rates (W m^{-3} s^{-1}). $D_{\mathrm{O_2}}^{\mathrm{eff}}$ (m^2 s^{-1}) represents effective diffusion coefficient of oxygen in the porous media, which is calculated by Bosanquet equation [24] summarized as follows:

$$D_{\mathrm{O_2}}^{\mathrm{eff}} = \frac{\varepsilon}{\xi}(\frac{1}{D_{\mathrm{O_2,N_2}}} + \frac{1}{D_{\mathrm{O_2,K}}}) \tag{6}$$

Where $D_{\mathrm{O_2,N_2}}$ and $D_{\mathrm{O_2,K}}$ represent binary diffusion and Knudsen diffusion coefficients, respectively:

$$D_{\mathrm{O_2,N_2}} = 0.018833\sqrt{\frac{1}{M_{\mathrm{O_2}}} + \frac{1}{M_{\mathrm{N_2}}}}\frac{T^{3/2}}{P\Omega_{\mathrm{D}}\zeta_{\mathrm{O_2,N_2}}^{2}} \tag{7}$$

$$D_{\mathrm{O_2,k}} = \frac{2}{3}\sqrt{\frac{8RT}{\pi M_{\mathrm{O_2}}}}r \tag{8}$$

Where M (kg mol^{-1}) is the mole weight of species. R is universal gas constant (J mol^{-1} K^{-1}). F is Faraday’s constant (C mol^{-1}). T (K) is operation temperature. It should be emphasized that the model is safely considered to be isothermal duo to thinner cathode structure thickness and small electrode surface area. P (Pa) is operation pressure. r represents average pore size of electrode microstructure which is evaluated by a so called 13-line method [37]. Average pore/particle sizes are computed by moving the specific line though the computational domain until non-pore/pore particle is reached. Totally thirteen different directions are chosen to compute the average pore diameter. These 13 different lengths are finally averaged to compute the effective pore/particle size. $\zeta_{\mathrm{O_2,N_2}}^{2}$ is the arithmetic mean value of $\zeta_{\mathrm{O_2}}^{2}$ and $\zeta_{\mathrm{N_2}}^{2}$. Ω_{D} is the collision integral calculated as:

$$\Omega_{\mathrm{D}} = 1.336\left(\frac{Tk}{\varepsilon}\right)^{-0.1814} \tag{9}$$

The values of diffusion coefficient related factors are listed in Table 2 [24].

Species	$\zeta\,(\mathring{A})$	ε/k (K)	M (kg mol^{-1})

O_2	3.54	88.0	31.9988×10^{-3}
N_2	3.68	91.5	28.0314×10^{-3}

Table 2 Diffusion parameters

3.2 Electrochemical model

The complex physical and electrochemical processes inside the electrode have dominant influence on the cell performance [21]. In the previous similar studies, charge transport was reflected though the concept of chemical potential according to the works of Matsuzaki K et al. [24] Y.T. Kim et al [38] and He A et al. [39], which show incapability to directly describe the relationship between polarization loss and electrochemical reaction rates. To address this issue, the governing equation of ionic and electronic overpotential are directly solved in this study:

$$\nabla \cdot \left(\kappa_{\mathrm{ion}} \nabla \varphi_{\mathrm{ion}} \right) = S_{\mathrm{ion}} \qquad (10)$$

$$\nabla \cdot \left(\kappa_{\mathrm{ele}} \nabla \varphi_{\mathrm{ele}} \right) = S_{\mathrm{ele}} \qquad (11)$$

Where φ_{ion} and φ_{ele} represent ionic and electronic overpotential. κ_{ion} and κ_{ele} are ionic and electronic conductivity of LSCF, which are dependent on O_2 local partial pressure and operating temperature. In this study, the relationship between electronic conductivity and O^{2-} chemical diffusion coefficient is based on the fitting curve from previous work of Matsuzaki K et al [24]. The experiment data used for curve fitting comes from work of Bouwmeester et al. [40].

$$\log_{10} \kappa_{\mathrm{ele}} = -0.0237 \left(\log_{10} p_{\mathrm{O_2}} \right)^2 + 0.0034 \log_{10} p_{\mathrm{O_2}} + 4.8126 \ \ (1073.15\mathrm{K}) \qquad (12)$$

$$\log_{10} \kappa_{\mathrm{ele}} = -0.0222 \left(\log_{10} p_{\mathrm{O_2}} \right)^2 - 0.0169 \log_{10} p_{\mathrm{O_2}} + 4.8065 \ \ (1023.15\mathrm{K}) \qquad (13)$$

$$\log_{10} \kappa_{\mathrm{ele}} = -0.0095 \left(\log_{10} p_{\mathrm{O_2}} \right)^2 - 0.0011 \log_{10} p_{\mathrm{O_2}} + 4.8152 \ \ (973.15\mathrm{K}) \qquad (14)$$

$$\log_{10}\kappa_{\mathrm{ele}} = -0.008\left(\log_{10} p_{\mathrm{O_2}}\right)^2 - 0.0024\log_{10} p_{\mathrm{O_2}} + 4.8447 \ \ (923.15\mathrm{K}) \tag{15}$$

$$\log_{10}\tilde{D} = -0.1765\left(\log_{10} p_{\mathrm{O_2}}\right)^2 - 0.2724\log_{10} p_{\mathrm{O_2}} - 9.2256 \ \ (1073.15\mathrm{K}) \tag{16}$$

$$\log_{10}\tilde{D} = -0.1884\left(\log_{10} p_{\mathrm{O_2}}\right)^2 - 0.3243\log_{10} p_{\mathrm{O_2}} - 9.4969 \ (1023.15\mathrm{K}) \tag{17}$$

$$\log_{10}\tilde{D} = -0.1882\left(\log_{10} p_{\mathrm{O_2}}\right)^2 - 0.2491\log_{10} p_{\mathrm{O_2}} - 9.7676 \ (973.15\mathrm{K}) \tag{18}$$

$$\log_{10}\tilde{D} = -0.1252\left(\log_{10} p_{\mathrm{O_2}}\right)^2 - 0.2051\log_{10} p_{\mathrm{O_2}} - 9.9554 \ (923.15\mathrm{K}) \tag{19}$$

Where $\tilde{D}$ is O^{2-} chemical diffusion coefficient. The ionic conductivity is reversed by the value of $\tilde{D}$:

$$\tilde{D} = \frac{1}{4F}\frac{\kappa_{\mathrm{ion}}\kappa_{\mathrm{ele}}}{\kappa_{\mathrm{ion}}+\kappa_{\mathrm{ele}}}\frac{\partial\mu_{\mathrm{O}}}{\partial c_{\mathrm{O}}} \approx -\frac{RTV_{\mathrm{m}}}{8F^2}\kappa_{\mathrm{ion}}\frac{\partial \ln p_{\mathrm{O_2}}}{\partial\delta} \tag{20}$$

$$\frac{\partial\delta}{\partial \ln p_{\mathrm{O_2}}} = -3.36260\times10^{-5}\cdot T + 2.59403\times10^{-2} \tag{21}$$

Where $V_{\mathrm{m}} = 35.5\times10^{-6}$ ($\mathrm{m^3\ mol^{-1}}$) is the mole volume of LSCF.

Surface reaction of MIEC electrode occurs at the gas/solid interface. The Butler–Volmer equation is introduced to describe the relationship between activation loss and reaction rates in terms of current density:

$$J = j_0\cdot\left[\exp\left(\frac{4\alpha F}{RT}\eta_{\mathrm{act}}\right) - \exp\left(-\frac{4\beta F}{RT}\eta_{\mathrm{act}}\right)\right] \tag{22}$$

Where J ($\mathrm{A\ m^{-3}}$) represents electrochemical reaction rates. α and β are the symmetry factors; η_{act} means active overpotential of electrodes which is calculated by:

$$\eta_{\mathrm{act}} = \varphi_{\mathrm{ion}} - \varphi_{\mathrm{ele}} \tag{23}$$

j_0 (A m^{-3}) represents the reference exchange current densities for oxygen reduction reaction rates.

$$j_0 = k_0 p_{O_2}^{\gamma} \exp\left(-\frac{1242.06}{R}\left(\frac{1}{T}-\frac{1}{T_0}\right)\right) \tag{24}$$

Where k_0 is the pre-exponential factor for the purpose of fitting experimental data. γ is the reaction order. It is clarified that the source terms of both charge transport and species transport are dependent on the electrochemical reaction rates, as is shown in Table 3:

Source terms	S_{ele}	S_{ion}	S
Value	$-J$	J	$-J/4\text{F}$

Table 3 Source terms

The electrochemical related parameters are shown in Table 4.

Parameters	α	β	γ	k_0	T_0
Value	0.3	0.25	0.2	3.4×10^{8}	1023 (K)

Table 4 Electrochemical factors

The performance of electrode is assessed by the ohmic polarization and activation polarization. Ohmic overpotential is measured by the difference between the import and export of ionic/electronic overpotential. Considering uneven distribution properties of activation loss inside solid phase, average activation overpotential is calculated by:

$$\eta_{\text{act,ave}} = \frac{\sum_{i=1}^{N}\eta_{\text{act}}}{N} \tag{25}$$

Where N is the total number of active solid phases.

4. Numerical method

4.1 Multiple-relaxation-time lattice Boltzmann method

The lattice Boltzmann method (LBM) is conducted to solve the coupled diffusion equations. The decoupling of the physical quantities from the governing equations is a key issue in the realization of the algorithm. For the species and charge transport process, the value of oxygen diffusion coefficient (1×10^{-5} magnitude) is generally 7-8 order magnitude lower than electronic conductivity (1×10^{3} magnitude), 3-4 order magnitude lower than ionic conductivity(1×10^{1}-1×10^{2} magnitude). To avoid the time step mismatch caused by different diffusion coefficient, shifting term transformation approach is creatively introduced by Mu et al. [41] which is expressed as:

$$\nabla\cdot\left(D_0\nabla\varphi_{\mathrm{ion}}\right)=\frac{D_0S_{\mathrm{ion}}}{\kappa_{\mathrm{ion}}} \tag{26}$$

$$\nabla\cdot\left(D_0\nabla\varphi_{\mathrm{ele}}\right)=\frac{D_0S_{\mathrm{ele}}}{\kappa_{\mathrm{ele}}} \tag{27}$$

Where D_0 is an introduced variable with the same magnitude as oxygen diffusion coefficient. The value of D_0 is set as 1×10^{-5} (m^2 s) in this study.

The diffusion governing equations above are discretized by lattice Boltzmann method (LBM) due to its advantage of dealing with complex boundary conditions. As diffusion coefficient and conductivity is mutative in real structures, the relaxation factors are constantly changing. Multiple-relaxation-time Lattice Boltzmann method (MRT-LBM) is adopted due to its numerical stability handling problems with variable relaxation factors. The evolution of distribution function (DF) is shown as follows:

$$f_i\left(x+e_i\delta t,t+\delta t\right)-f_i\left(x,t\right)=-M^{-1}\Lambda\left(m\left(x,t\right)-m_i^{\mathrm{eq}}\left(x,t\right)\right) \tag{28}$$

Where f_i is distribution function. e_i is discretized velocity. M is the transformation matrix. m_i means transformed distribution function thus m_i^{eq} is transformed equilibrium distribution function.

Λ is relaxation matrix. t and x are time and mesh interval. In present study, the D3Q7 (7 velocities and 3 dimensions) is conducted for numerical simulation, the reliability of which has been widely proved in lots of previous literatures to deal with diffusion problems [41]-[44]. Detailed information of D3Q7 model is presented in Figure 2(a). The 7 discrete velocities are expressed as:

$$\left[e_0,\ e_1,\ e_2,\ e_3,\ e_4,\ e_5,\ e_6\right]=\begin{bmatrix} 0 & 1 & -1 & 0 & 0 & 0 & 0 \\ 0 & 0 & 0 & 1 & -1 & 0 & 0 \\ 0 & 0 & 0 & 0 & 0 & 1 & -1 \end{bmatrix} c \tag{29}$$

where c is defined as lattice velocity that is calculated by: $c=\Delta x/\Delta t$. The transformation matrix is defined as:

$$M=\begin{bmatrix} 1 & 1 & 1 & 1 & 1 & 1 & 1 \\ 0 & 1 & -1 & 0 & 0 & 0 & 0 \\ 0 & 0 & 0 & 1 & -1 & 0 & 0 \\ 0 & 0 & 0 & 0 & 0 & 1 & -1 \\ 6 & -1 & -1 & -1 & -1 & -1 & -1 \\ 0 & 2 & 2 & -1 & -1 & -1 & -1 \\ 0 & 0 & 0 & 1 & 1 & -1 & -1 \end{bmatrix} \tag{30}$$

The weight coefficient is given as:

$$\omega_\alpha=\begin{cases} j_0 & i=0 \\ \dfrac{1-j_0}{6} & i\neq 0 \end{cases} \tag{31}$$

Where $j_0=0.25$. The relaxation diagonal matrix Λ is expressed as:

$$\Lambda=\mathrm{diag}[1,\ \mathrm{s}_1,\ \mathrm{s}_1,\ \mathrm{s}_1,\ s_4,\ s_5,\ s_6] \tag{32}$$

$$s_1=s_2=s_3=\frac{1}{\tau} \tag{33}$$

$$s_4=s_5=s_6=\frac{1}{0.5+\dfrac{1}{6\ \tau-0.5}} \tag{34}$$

Where τ is the relaxation coefficient with the range of $0 \leq \tau < 2$ to ensure numerical stability, which is calculated by [24]:

$$\tau = 0.5 + \frac{2D_0}{1 - j_0} \frac{dt}{dx^2} \tag{35}$$

4.2 Boundary condition and numerical strategy

The porous domain consists of 250×70×70 voxels which is simulated to sinter at a constant temperature of 1000 °C for 1000 KMC steps while the resolution of each pixel is 100nm [38], as is shown in Figure 1. A buffer domain with a thickness of 2 μm is set on the front and back of the porous media, inside which oxygen, electron and ion can directly pass though so as to optimize calculation stability. It is defined that two sides of the computational domain are directly connected with the flow channel and electrolyte. The total lattice elements of the pore phase under different electrode microstructures illustrated in this study varies from 490000-735000 (porosity 0.4-0.6) which is closely dependent on sintering time and initial compact powders. Moreover, it should be mentioned that time and mesh interval are defined as 5×10^{-10} s. and 1×10^{-7} m, respectively.

Periodic boundary condition is applied to describe the boundary conditions around the y-axis and z-axis. For O_2 diffusion process along x direction, the boundary condition is defined as:

$$\begin{cases} C = C_0 & x = 0 \\ \dfrac{\partial C}{\partial x} = 0 & x = L \end{cases} \tag{36}$$

Constant voltage method shows incapability to deal with half-cell model since ionic and electronic overpotential lack mutual restriction at constant voltage conditions. Therefore, constant current density is always used to limits the inlet flux of ionic and electronic overpotential:

$$\begin{cases} \kappa_{\text{ele}} \dfrac{\partial \varphi_{\text{ele}}}{\partial x} = -I & x = 0 \\ \dfrac{\partial \varphi_{\text{ele}}}{\partial x} = 0 & x = L \end{cases} \tag{37}$$

$$\begin{cases} \dfrac{\partial \varphi_{\text{ion}}}{\partial x} = 0 & x = 0 \\ \kappa_{\text{ion}} \dfrac{\partial \varphi_{\text{ion}}}{\partial x} = I & x = L \end{cases} \tag{38}$$

Where I is the working current density of electrode. The discrete format for Neumann boundary is defined as:

For electronic overpotential:

$$f_i\left(x_\alpha, t\right) = C\left(x_\alpha, t\right) - \sum_{j=0,\, j\neq i}^{6} f_j\left(x_\alpha, t\right) - \frac{I\Delta x}{\kappa_{\text{ele}}} \tag{39}$$

For ionic overpotential:

$$f_i\left(x_\alpha, t\right) = C\left(x_\alpha, t\right) - \sum_{j=0,\, j\neq i}^{6} f_j\left(x_\alpha, t\right) + \frac{I\Delta x}{\kappa_{\text{ion}}} \tag{40}$$

The computational procedure of LBM is exhibited in Figure 2 (b). For LB simulation, the macroscale factors are firstly discrete into different distribution functions along the velocity direction of fractious particles (7 velocities and 3 dimensions in this study). These DFs stream along a given direction and collide at the lattice sites. In the last step of LB method, the distribution functions should be converted to macroscale factors for further evaluation of the real physical properties' distribution inside the simulation space. Then, other resultant quantities such as electrochemical reaction rates, activation overpotential and ohmic loss etc. can be easily calculated in the light of above updated real physical properties. It should be noted that the simulation is achieved by GPU based parallel computation. Computation process is simply divided into three steps. Firstly, the real microstructure of LSCF porous electrode is reconstructed by KMC sintering model. Model related variables should also be initialized at first. Secondly, the computing module is carried out to sequentially update the macro-properties of O_2 concentration, electronic and ionic overpotential. It is important to point out that source terms are updated each time when the computing module is processed. The coupled update of source terms is the driving force for model convergence. Thirdly, as the calculation progresses, simulation tends to be stable. The model should meet the principle that ionic and electronic current density calculated by internal reaction rates should equal to inlet current density flux to confirm conservation of the prediction model, that is:

$$I = \frac{\sum J_{\text{ele}} \left(\Delta x\right)^3}{A} = \frac{\sum J_{\text{ion}} \left(\Delta x\right)^3}{A} \tag{41}$$

Where A (m^2) means cross section area. What needs to be clarified is that Eq.41 is proposed as an optimal criterion for convergence judgement. This criterion focuses on the conservation characteristics inside porous electrode that is generally most challenging for pore scale electrochemical models. Although extensive research works have been carried out on electrochemical model based on pore scale LBM studies [24], [39], [41], no study gave clear clarification for the convergence principle. In the present study, the error is set not more than 0.1% to ensure convergence. The specific criterions for convergence judgement are listed as follows:

$$\frac{I - \frac{\sum J_{\text{ele}} \left(\Delta x\right)^3}{A}}{I} \le 0.1\% \tag{42}$$

$$\frac{I - \frac{\sum J_{\text{ion}} \left(\Delta x\right)^3}{A}}{I} \le 0.1\% \tag{43}$$

5. Result and discussion

5.1 Experimental comparison

The validation of KMC method is necessary to ensure the reliability of reconstruction electrode. The initial powders are simulated to sinter at a constant temperature of 1000 °C for 60000 KMC steps (mcs). It is clearly to found that the KMC method could precisely simulate electrode densification behavior and specific surface area evolution at a real time scale, as can be seen in Figure 3(a) and (b) [12]. It takes 10 mins physical sintering time to increase relative density of LSCF from 0.703 to 0.806 in accordance with Yan at al.'s previous experiments [12], which is realized by 3000 KMC steps by our KMC model. Therefore, the correction coefficient between KMC step and physical sintering time could be calculated by: $\Gamma = 600\ \mathrm{s} / 3000\ \mathrm{mcs}=0.2\ \mathrm{s\ mcs}^{-1}$. It means that 1 mcs is equivalent to 0.2 s physical time in this study.

Numerical results of LB method are also comprehensively compared with experimental data to prove the reliability of LBM model [24]. It should be demonstrated that the reconstructed electrode exhibits an effective surface area of $5.65\,\mu\mathrm{m}^2\ \mu\mathrm{m}^{-3}$ with a porosity of 0.44. For the lack of the detailed information on the microstructures and sintering conditions, the consistence of reconstructed electrode with experimental sample is not considered in the present study. The thickness of reconstructed electrode for model validation is set to equal with experiment ones while the real porous backbones are reconstructed by the KMC method, the reliability of which has been comprehensively validated in Figure 3(a) and (b). We believe the comparison can serve as a comprehensive model evaluation to confirm that the results are reasonable. As is shown in Figure 3(c), the predicted overpotential show good agreement with experimental results under different O_2 mole fraction. Figure 3(d) shows that simulation adapts well to temperature changes.

5.2 Influence of O_2 partial pressure

According to the previous work of H. J. M. Bouwmeester et al., the ionic conductivity of LSCF material decreases markedly as the oxygen partial pressure below 10^{-2} bar [40]. However, the effects of local O_2 particle pressure on electrode performance were rarely discussed. In this section, the O_2 partial pressure varies from 0-1 bar to fully investigate its effects on cell performance. As is shown in Figure 4 (a) and (b), it is clear that O_2 partial pressure plays significant roles in ohmic and active polarization when local O_2 partial pressure below 10^{-1} bar. The high ohmic loss at $p_{\mathrm{O_2}} < 0.1\ \mathrm{bar}$ is obviously induced by low ionic conductivity. As O_2 partial pressure becomes higher than 0.1 bar, ohmic loss shows slight increase which might be caused by conductivity curve fitting error. From a general point of view, as O_2 partial pressure keep on increasing, ohmic loss become almost unaffected by O_2 partial pressure in the sub-range of $p_{\mathrm{O_2}} > 0.1\ \mathrm{bar}$. Lack of O_2 is the main reason for high activation overpotential. Different from ohmic loss, activation polarization shows significant drops as $p_{\mathrm{O_2}} > 0.1\ \mathrm{bar}$ since high O_2 concentration makes electrochemical reactions much easier to occur.

It is worth noting that influential minimum pressure (0.1 bar) shows slight inconsistence with experimental results (0.01 bar) [40]. It is might because that experimental test is not based on real fuel cell working environment. The measurement does not consider O_2 diffusion resistance and electrochemical consumptions. Taken together, the discussion above highlights the importance of O_2 partial pressure on electrode performance. Considering that insufficient O_2 supply conditions such as high current density and uneven flow field distribution conditions is unavoidable inside electrodes, it is suggested that influence of O_2 partial pressure on conductivity should not be neglected, especially for the full fuel cell CFD flow field simulations.

5.3 Influence of sintering kinetics

O_2 concentration, ionic and electronic overpotential distribution in LSCF electrode are exhibited in Figure 5. As expected, since the cathode thickness is small, the variation range of O_2 concentration along the depth is narrow. Therefore, the oxygen concentration has a very limited effect on the reaction rate and overpotential. For comparison, the ohmic resistance due to the transport of oxygen ions (O^{2-}) through the oxygen-ion conducting particles from the porous cathode to the dense electrolyte is much more significant, which causes the electrochemical reaction to mainly take place in a small region near the electrolyte [45]. In accordance with B-V equations, if we want to get more electrochemical reactions from the fuel cell, we have to lose voltage as the price. The higher activation overpotential is consumed at the region to further support the high electrochemical reaction rates. Even though electronic overpotential shows obviously gradient along the *x* direction, electronic overpotential is found to have little impacts on cell performance due to excellent electronic conductivity of LSCF. Ionic overpotential shows significant influence on electrode performance owing to lower ionic conductivity of LSCF materials. It is indicated that the electrode performance is deeply affected by electrode ionic conductivity, which is mainly dependent on material properties as well as electrode fabrication method. The transport properties (electronic/ionic conductivities) of the porous electrode can be improved by developing novel electrode materials or by optimizing the electrode microstructures. In the present study, we focus on electrode microstructure optimization for performance enhancement.

Figure 6 shows the effects of initial grain size on electrode performance. The grain size of LSCF initial powder is varied from 0.2μm to 0.3μm and 0.4μm and sintered for 500 KMC steps. It is apparent from Figure 6 (a) that initial grain size shows significant effects on activation potential since small initial particle size could provide more active reaction sites after sintering. Interestingly, the maximum electrochemical reaction rate, as is shown in Figure 6 (b), appears at the place near the electrolyte, whereas not at the nearest interface. The most likely causes of this phenomenon is the particle deposition caused by sintering, which more or less decrease the effective reaction sites at the place nearby the electrolyte.

In practice, the size of the starting particles is usually not uniform. Thus, it is necessary to investigate the effects of initial particle size distribution on electrode polarization. As can be seen in Figure 7 (a) and (b), the existence of several oversized particles inside the sintered electrode increases the sintering difficulty and largely hinders the formation of active reaction sites. Compared with uniform initial powders, non-uniform ones tend to increase the activation loss substantially. Uniform grain sizes at 0.3μm even perform better than non-uniform powders with an average particle radius of 0.2μm. Moreover, reaction rates of initial powder with poor consistency also show significant unevenness while larger reaction rates are needed to get the desirable current density, as can be seen in Figure 7(c). In contrast to earlier findings [12][46][47], the results above strongly indicate that consistency of primary particles even plays a more important roles than initial particle radius for electrode performance. It is proposed that much more attention should be paid to the uniformity of powder compacts fabrication rather than reduce average particle size.

Another inevitable factor indued by fabrication procedure is the shape of compact powder. For simplification, initial powder is assumed as sphere in most of literature studies [12], [14], [35], which ignores the plate-like features of those particles. The discrete element method-based code proposed in Refs [46] is carried out to consider the irregularly shaped compact powder in present study. The reconstructed irregular powder is exhibited in Figure 8(a). It is easy to count that a greater number of irregular particles (2727 particle) is required to fill the same space than regular ones (2252 particles). What can be clearly seen in Figure 8 (b) is that irregular particles are beneficial for reducing activation overpotential of electrode owing to relatively more initial reaction area. Irregular particles more or less likely contribute to reducing reaction rate fluctuations, as can be seen in Figure 8 (c). Considering that effective reaction area tends to decrease owing to sintering densification, the initial effective reaction area generated by compact powder should become a major factor that helps optimize electrode performance.

Above discussions mainly focus on the influence of initial compact powder while the effects of sintering process are not involved. In this section, the KMCs simulation is performed 2000 steps while sintering structures are recorded every 100 KMC steps to get real structure under different sintering stages. As is shown in Figure 9, it is interesting to found that ohmic loss shows obviously decrease in the early stage of sintering. Observed reduction of ohmic overpotential could be mainly attributed to enhancement of electrode connectivity while the impacts of porosity are not significant. As sintering processes, the ohmic loss tends to become stable, which means that excessive sintering cannot further improve electrode conductivity. The most interesting finding is that porosity is not suitable for quantifying the conductivity changes. However, in the previous modeling studies, porosity is generally regarded as an important correction for conductivity [49][50]:

$$\kappa = \left(1-\varepsilon\right)\kappa_0 \tag{44}$$

$$\kappa = \frac{\left(1-\varepsilon\right)}{\tau}\kappa_0 \tag{45}$$

Where κ_0 represents pure conductivity of materials. This is an important issue that needs clarification for future research. As can be seen in Figure 9 (a), the correction principle shown in Eq. 43 can't accurately describe the influence of porous media on ionic and electronic conductivity during sintering process. The correction principle shown as Eq. 45 which reasonably takes tortuosity into account is therefore recommended to further reveal the relationship between conductivity and porous media. The connectivity of electrode is proved to have dominant influence on electrode conductivity which is closely related with sintering kinetics and should not be regarded as an empirical parameter for modeling studies [47], [50]-[52]. Moreover, as can be seen in Figure 9 (b), activation overpotential keeps increasing as sintering processes, which could be explained by the grain-coarsening caused by high temperature. Reduction of active reaction sites also leads to an increase of electrochemical reaction rate inside the electrode to a certain extent. In summary, above results suggest that there is a tight association between sintering process and oxygen reduction reaction (ORR) activities. On the one hand, sintering promotes the enhancement of electrode connectivity and stability thereby contributes to the reduction of ohmic loss. On the other hand, sintering is harmful for the formation of effective reaction interface. Since sintering is indispensable for obtaining a stable electrode structure, much more attention should be paid on the increase of electrochemical reaction sites of MIEC electrode.

5.4 Infiltrating technique for MIEC electrode

In accordance with discussion above, sintering will inevitably result in low ORR activities, which further emphasizes the necessity to promote the formation of reaction area. To improve the performance of the MIEC electrodes, the deposition of nano electrocatalysts based on infiltration technique has been widely demonstrated in pervious experimental studies [53]-[55]. However, the model studies based on infiltrated microstructure reconstruction are rarely found in literatures. In this section, a reconstruction method proposed by Zhang et al [27] is introduced to simulate the infiltration process of preexisting MIEC electrode (backbone structure) while LSCF nanoparticles are randomly infiltrated onto the surface of preexisting electrode. The contact between the backbone structure and infiltrated nanoparticles are controlled by contact angel with a common value of 120°. For simplicity, it is hypothesized that nanoparticles are hemispheres. The main challenge for infiltrated process is the aggregation phenomenon to generate uniform covered infiltration surface. A weighting factor λ is proposed to evaluate the risks of aggregation formation:

$$P_{\mathrm{TS}} = \frac{\lambda A_{\mathrm{TS}}}{\lambda A_{\mathrm{TS}} + \left(1-\lambda\right) A_{\mathrm{NS}}} \tag{46}$$

Where A_{TS} represents surface area after infiltration. A_{NS} means surface area of nanoparticles. The probability that a nanoparticle covers another infiltrated nanoparticle is defined as:

$$P_{\mathrm{NS}} = 1 - P_{\mathrm{TS}} \tag{47}$$

It should be mentioned that nanoparticle size is generally not more than 100nm therefore the resolution of 100nm cannot meet the demand of nanoscale simulation anymore. The resolution is redefined as 5nm to provide detailed information of infiltrated electrode. A computational domain of 280×280×280 voxels is presented to evaluate the influence of infiltration process. It is apparent from Figure 10 (a) and (b) that there is a significant improvement if traditional preexisting electrode is infiltrated by nanoparticles since infiltration electrode has more active reaction sites compared with traditional ones. The most important aspect to emerging from the Figure 10 (b) is that infiltration electrodes could obviously promote the evenness of reaction rates distribution since reaction sites are more evenly distributed inside an infiltration electrode. The most likely cause of homogenization of reaction sites is that nanoparticles tend to fill up areas of large pores thus the ORR performance could also be further improved.

Figure 11 illustrates the effects of nanoparticle size on electrode performance. It is easy to understand that smaller nanoparticles result in a larger reaction area. Therefore, lower active polarization and more uniform ORR activates could be achieved with smaller nanoparticles, as is shown in Figure 11 (a) and (b). However, in practice, the size of nanoparticles may not be too small to ensure reasonable fabrication cost and good durability. Therefore, the development of cost-effective fabrication process for nanostructured electrodes with suitable nanoparticles should be encouraged.

In terms of infiltration loading that used to describe the amounts of nanoparticles, the performance with different loading (5%, 10%, 15%) are presented in Figure 12. There is an obvious reduction of overpotential polarization along with the increasing of infiltration load, as is shown in Figure 12 (a). Relatively large value of infiltration load gives rise to more active reaction sites, which is the major reason for polarization reduction. With successive increases of the infiltration load, more and more large size pores are filled with nanoparticles (Figure 12 (a)), which provides direct evidence that infiltration load is an important factor that affects homogenization of reaction sites distribution. However, it should be clarified that with the increase of numerical infiltration load (>15%), even though the same constant flux boundary is given to predict the final polarization loss, infiltrated electrode can no longer produce an equivalent electrochemical reaction rates inside porous media due to the lack of O_2. That indicates that infiltrated electrode with high nanoparticle load has difficulties operating at high current densities. Aggregation of nanoparticles starts to become inevitable at relative high infiltration loading once the interface of preexisting electrode is almost covered by nanoparticles. It is obvious to see that electrode with 15% loading generates more isolated sites than 5% load ones, which is harmful for the stability of electrode structure. Moreover, as infiltration loading increases from 10% to 15%, the polarization loss merely shows a slight decrease from 0.289704 V to 0.270978 V. Taken together, it is proposed that a moderate load around 10% (R_{inf}= 25nm) would be sufficient to improve electrode performance. In addition, it is worth to note that different nanoparticle size corresponds to different optimal infiltration load.

What should be clarified is that most of previous modeling studies in the field of infiltrated electrode have only focused on the amount of electrochemical reaction sites [36, 39] but ignored O_2 supply, all of which fails to give an accurate prediction for the selection of optimal infiltration load. This also demonstrates the necessity to develop pore scale LBM model based on real microstructure reconstruction.

6. Conclusion

In the present study, a Kinetic Monte Carlo method is established for numerical reconstruction of porous backbones of LSCF electrode. a pore-scale Lattice Boltzmann method is undertaken to describe the transport properties and coupling effects of ORR activities inside the porous media. The prediction results show good agreement with experimental data. The present study provides the first comprehensive pore scale assessment of O_2 local partial pressure and sintering kinetics on cell performance. This work also offers valuable insights into infiltrated electrode to overcome the low ORR activities caused by sintering. The main conclusions are listed as follows:

(1) Local O_2 partial pressure plays unneglected roles in the ohmic loss of LSCF electrode at the interval of $p_{\mathrm{O_2}} < 0.1\ \mathrm{bar}$ while its influence on active polarization is more continuous and not limited by above ranges.

(2) Initial states of sintering precursor remarkably contribute to the electrochemical performance of LSCF electrode. Large initial reaction area resulting from relatively small initial particle size is meaningful for the sintered electrode performance. Exists of oversized particles tend to hinder the formation of active reaction sits and it is emphasized that that

consistency of primary particles even plays a more vital roles than initial particle size for electrode performance. Irregular particles are found to be beneficial for reducing activation overpotential of electrode.

(3) By investigating the electrochemical performance of reconstructed electrode at different sintering stages, it is found that ohmic loss shows obviously decrease in the early stage of sintering which is mainly dominated by the enhancement of electrode connectivity rather than porosity. It is clarified that the correction principle that merely square up porosity can't accurately describe the influence of porous media on material conductivity. Owing to grain-coarsening phenomenon caused by sintering, activation overpotential keeps increasing as sintering processes.

(4) The infiltrated technique is one of the more practical ways to further improve the ORR performance of electrode. Infiltration electrode could effectively solves the problem of insufficient reaction area caused by sintering and promotes uniform distribution of reaction rate to a large extent. Even though smaller size and larger infiltration load of nanoparticles are found to be better for cell performance, these findings are somewhat idealistic and limited by manufacture crafts. In addition, the selection of optimal infiltration load is closely related with nanoparticle size while the influence of O_2 supplement should also be fully taken into account.

Acknowledgements

This work is supported by the National Key Research and Development Program of China (2017YFB0601904) and the Natural Science Foundation for Outstanding Young Scholars of Tianjin (18JCJQJC46746700). M. NI also thanks the grants (Project Number: PolyU 152214/17E and PolyU 152064/18E) from Research Grant Council, University Grants Committee, Hong Kong SAR.

Reference

[1] M. Ni, Z. Shao. Fuel cells that operate at 300° to 500°C. Science 2020; 369(6500): 138-139. https://doi.org/10.1126/science.abc9136.

[2] H. Su, Y. Hu. Progress in low-temperature solid oxide fuel cells with hydrocarbon fuels. Chemical Engineering Journal, 2020: 126235. https://doi.org/10.1016/j.cej.2020.126235.

[3] Z. Lyu, Y. Wang, Y. Zhang, M. Han. Solid oxide fuel cells fueled by simulated biogas: Comparison of anode modification by infiltration and reforming catalytic layer. Chemical Engineering Journal, 2020, 393: 124755. https://doi.org/10.1016/j.cej.2020.124755.

[4] W.K. Evans, K. Rattanakornkan, A. Suksangpanomrung, S. Charojrochkul. The simulations of tubular solid oxide fuel cells (SOFCs). Chemical engineering journal, 2011, 168(3): 1301-1310. https://doi.org/10.1016/j.cej.2011.02.034.

[5] H. Xu, J. Ma, P. Tan, B. Chen, Z. Wu, Y. Zhang, H. Wang, J. Xuan, M. Ni. Towards online optimisation of solid oxide fuel cell performance: combining deep learning with multi-physics simulation. Energy and AI, 2020: 100003. https://doi.org/10.1016/j.egyai.2020.100003

[6] T.J. Huang, M.C. Huang, W.J. Chen, C.L. Chou. Oscillation of electrical current during direct methane oxidation over Ni-added LSCF–GDC anode of solid oxide fuel cells. Chemical Engineering Journal, 2009, 153(1-3): 164-169. https://doi.org/10.1016/j.cej.2009.06.014

[7] Y. Zheng, C. Zhao, T. Wu, Y. Li, W. Zhang, J. Zhu, G. Geng, J. Chen, J. Wang, B. Yu, J.

Zhang. Enhanced oxygen reduction kinetics by a porous heterostructured cathode for intermediate temperature solid oxide fuel cells. Energy and AI, 2020, 2: 100027. https://doi.org/10.1016/j.egyai.2020.100027

[8] I. Riess. Mixed ionic–electronic conductors-material properties and applications. Solid State Ionics, 2003, 157(1-4): 1-17. https://doi.org/10.1016/S0167-2738(02)00182-0

[9] Z. Yan, S. Hara, N. Shikazono. Towards a realistic prediction of sintering of solid oxide fuel cell electrodes: From tomography to discrete element and kinetic Monte Carlo simulations. Scripta Materialia 146 (2018): 31-35. https://doi.org/ 10.1016/j.scriptamat.2017.10.035

[10] T.T. Molla, R. Bjørk, E. Olevsky, N. Pryds, H.L. Frandsen. Multi-scale modeling of shape distortions during sintering of bi-layers. Computational materials science 88 (2014): 28-36. https://doi.org/10.1016/j.commatsci.2014.02.041

[11] P.R. Shearing, Q. Cai, J.I. Golbert, V. Yufit, C.S. Adjiman, N.P. Brandon. Microstructural analysis of a solid oxide fuel cell anode using focused ion beam techniques coupled with electrochemical simulation. Journal of Power Sources 195.15 (2010): 4804-4810. https://doi.org/10.1016/j.jpowsour.2010.02.047

[12] Z. Yan, Y. Kim, S. Hara, N. Shikazono. Prediction of La0. 6Sr0. 4Co0. 2Fe0. 8O3 cathode microstructures during sintering: Kinetic Monte Carlo (KMC) simulations calibrated by artificial neural networks. Journal of Power Sources 346 (2017): 103-112. https://doi.org/10.1016/j.jpowsour.2017.02.029

[13] B. Kenny, M. Valdmanis, C. Baker, J.G. Pharoah, K. Karan. Computation of TPB length, surface area and pore size from numerical reconstruction of composite solid oxide fuel cell electrodes. Journal of Power Sources, 2009, 189.2: 1051-1059. https://doi.org/ 10.1016/j.jpowsour.2008.12.145

[14] Y. Wang, C. Wu, Q. Du, M. Ni, K. Jiao, B. Zu. Morphology and performance evolution of anode microstructure in solid oxide fuel cell: A model-based quantitative analysis. Applications in Energy and Combustion Science 5 (2021): 100016. https://doi.org/10.1016/j.jaecs.2020.100016

[15] B. Prakash, S.S. Kumar, S.T. Aruna. Properties and development of Ni/YSZ as an anode material in solid oxide fuel cell: a review. Renewable and Sustainable Energy Reviews 36 (2014): 149-179. https://doi.org/10.1016/j.rser.2014.04.043

[16] Z. Yan, A. He, S. Hara, N. Shikazono. Modeling of solid oxide fuel cell (SOFC) electrodes from fabrication to operation: Microstructure optimization via artificial neural networks and multi-objective genetic algorithms. Energy Conversion and Management, 2019, 198: 111916. https://doi.org/10.1016/j.enconman.2019.111916

[17] M. Shah, P.W. Voorhees, S.A. Barnett. Time-dependent performance changes in LSCF-infiltrated SOFC cathodes: The role of nano-particle coarsening. Solid State Ionics, 2011, 187(1): 64-67. https://doi.org/10.1016/j.ssi.2011.02.003

[18] D. Rembelski, J.P. Viricelle, L. Combemale, M. Rieu. Characterization and comparison of different cathode materials for SC-SOFC: LSM, BSCF, SSC, and LSCF. Fuel Cells, 2012, 12(2): 256-264. https://doi.org/10.1002/fuce.201100064

[19] M. Letilly, O. Joubert, A.L.G.A. Salle. Characterisation and optimisation of the cathode/electrolyte couple for SOFC LSCF/BIT07. Journal of Power Sources, 2012, 212: 161-168. https://doi.org/10.1016/j.jpowsour.2012.03.042

[20] W.C. Jung, H.L. Tuller. A New Model Describing Solid Oxide Fuel Cell Cathode Kinetics: Model Thin Film SrTi1-xFexO3-δ Mixed Conducting Oxides–a Case Study. Advanced

Energy Materials, 2011, 1(6): 1184-1191. https://doi.org/10.1002/aenm.201100164

[21] F. Ciucci, W.C. Chueh, D.G. Goodwin, S.M. Haile. Surface reaction and transport in mixed conductors with electrochemically-active surfaces: a 2-D numerical study of ceria. Physical Chemistry Chemical Physics, 2011, 13(6): 2121-2135. https://doi.org/10.1039/C0CP01219J

[22] J Fleig, J Maier. The polarization of mixed conducting SOFC cathodes: Effects of surface reaction coefficient, ionic conductivity and geometry. Journal of the European Ceramic Society, 2004, 24(6): 1343-1347. https://doi.org/10.1016/S0955-2219(03)00561-2

[23] M. Gong, R.S. Gemmen, X. Liu. Modeling of oxygen reduction mechanism for 3PB and 2PB pathways at solid oxide fuel cell cathode from multi-step charge transfer. Journal of Power Sources, 2012, 201: 204-218. https://doi.org/10.1016/j.jpowsour.2011.11.002

[24] K. Matsuzaki, N. Shikazono, N. Kasagi. Three-dimensional numerical analysis of mixed ionic and electronic conducting cathode reconstructed by focused ion beam scanning electron microscope. Journal of Power Sources, 2011, 196(6): 3073-3082. https://doi.org/10.1016/j.jpowsour.2010.11.142

[25] J.M. Vohs, R.J. Gorte. High‐performance SOFC cathodes prepared by infiltration. Advanced Materials, 2009, 21(9): 943-956. https://doi.org/10.1002/adma.200802428

[26] D. Ding, X. Li, S. Y. Lai, K. Gerdes, M. Liu. Enhancing SOFC cathode performance by surface modification through infiltration. Energy & Environmental Science, 2014, 7(2): 552-575. https://doi.org/10.1039/C3EE42926A

[27] Y. Zhang, Q. Sun, C. Xia, M. Ni. Geometric properties of nanostructured solid oxide fuel cell electrodes. Journal of The Electrochemical Society, 2013, 160(3): F278. https://doi.org/10.1149/2.057303jes

[28] X. Shan, H. Chen. Lattice Boltzmann model for simulating flows with multiple phases and components. Physical review E, 1993, 47(3): 1815. https://doi.org/10.1103/PhysRevE.47.1815

[29] S. Chen, B. Yang, C. Zheng. A lattice Boltzmann model for heat transfer in porous media[J]. International Journal of Heat and Mass Transfer, 2017, 111: 1019-1022. https://doi.org/10.1016/j.ijheatmasstransfer.2017.04.054

[30] J. Wu. Two-phase Flow Dynamics in Two Parallel Thin Micro-channels. UC Irvine, 2020. escholarship.org/uc/item/0tp7c4j0

[31] C.K. Aidun, J.R. Clausen. Lattice-Boltzmann method for complex flows. Annual review of fluid mechanics, 2010, 42: 439-472. https://doi.org/10.1146/annurev-fluid-121108-145519

[32] H. Li, C. Pan, C.T. Miller. Pore-scale investigation of viscous coupling effects for two-phase flow in porous media. Physical Review E, 2005, 72(2): 026705. https://doi.org/10.1103/PhysRevE.72.026705

[33] R.A. Patel, J. Perko, D. Jacques, G.D. Schutter, G. Ye, K.V. Breugeld. A three-dimensional lattice Boltzmann method based reactive transport model to simulate changes in cement paste microstructure due to calcium leaching. Construction and Building Materials, 2018, 166: 158-170. https://doi.org/10.1016/j.conbuildmat.2018.01.114

[34] S.G. Lee, D.H. Jeon, B.M. Kim, J.H. Kang, C.J. Kim. Lattice Boltzmann simulation for electrolyte transport in porous electrode of lithium ion batteries. Journal of The Electrochemical Society, 2013, 160(4): H258. https://doi.org/10.1149/2.017306jes

[35] Y. Zhang, C. Xia, M. Ni. Simulation of sintering kinetics and microstructure evolution of composite solid oxide fuel cells electrodes. International journal of hydrogen energy, 2012, 37(4): 3392-3402. https://doi.org/10.1016/j.ijhydene.2011.11.020

[36] R.C. Gonzalez, R.E. Woods, S.L. Eddins. Digital image processing using MATLAB. Pearson Education India, 2004. https://dl.acm.org/doi/10.5555/993475

[37] K.J. Lange, P.C. Sui, N. Djilali. Pore scale simulation of transport and electrochemical reactions in reconstructed PEMFC catalyst layers. Journal of The Electrochemical Society, 2010, 157(10): B1434. https://doi.org/10.1149/1.3478207

[38] Y.T. Kim, Z. Jiao, N. Shikazono. Evaluation of La0. 6Sr0. 4Co0. 2Fe0. 8O3-Gd0. 1Ce0. 9O1. 95 composite cathode with three dimensional microstructure reconstruction. Journal of Power Sources, 2017, 342: 787-795. https://doi.org/10.1016/j.jpowsour.2016.12.113

[39] A. He, J. Onishi, N. Shikazono. Numerical Optimization of the Solid Oxide Fuel Cell Electrode-Electrolyte Interface Structure with Adjoint Method. ECS Transactions, 2019, 91(1): 2045. https://doi.org/10.1149/09101.2045ecst

[40] H.J.M. Bouwmeester, M.W. Den Otter, B.A. Boukamp. Oxygen transport in $La_{0.6}Sr_{0.4}Co_{1-y}Fe_yO_{3-\delta}$. Journal of Solid State Electrochemistry, 2004, 8(9): 599-605. https://doi.org/10.1007/s10008-003-0488-3

[41] Y. Mu, A.Z. Weber, Z. Gu, W. Tao. Mesoscopic modeling of transport resistances in a polymer-electrolyte fuel-cell catalyst layer: Analysis of hydrogen limiting currents. Applied Energy, 2019, 255: 113895. https://doi.org/10.1016/j.apenergy.2019.113895

[42] J. Lu, H. Lei, C. Dai. Analysis of the typical unified lattice Boltzmann models and a comprehensive multiphase model for convection-diffusion problems in multiphase systems. Physical Review E, 2019, 100(1): 013307. https://doi.org/10.1103/PhysRevE.100.013307

[43] H. Yoshida, M. Nagaoka. Multiple-relaxation-time lattice Boltzmann model for the convection and anisotropic diffusion equation. Journal of Computational Physics, 2010, 229(20): 7774-7795. https://doi.org/10.1016/j.jcp.2010.06.037

[44] L. Li, R. Mei, J.F. Klausner. Lattice Boltzmann models for the convection-diffusion equation: D2Q5 vs D2Q9. International Journal of Heat and Mass Transfer, 2017, 108: 41-62. https://doi.org/10.1016/j.ijheatmasstransfer.2016.11.092

[45] M. Ni, M.K.H Leung, D.Y.C Leung. Micro-scale modelling of solid oxide fuel cells with micro-structurally graded electrodes. Journal of Power Sources, 2007, 168(2): 369-378. https://doi.org/10.1016/j.jpowsour.2007.03.005

[46] D. Chen, Z. Lin, H. Zhu, R.J. Kee. Percolation theory to predict effective properties of solid oxide fuel-cell composite electrodes. Journal of Power Sources, 2009, 191(2): 240-252. https://doi.org/10.1016/j.jpowsour.2009.02.051

[47] C. Wu, Z. Yang, S. Huo, A.U.H. Najmi, Q. Du, K. Jiao. Modeling and optimization of electrode structure design for solid oxide fuel cell. International Journal of Hydrogen Energy, 2018, 43(31): 14648-14664. https://doi.org/10.1016/j.ijhydene.2018.05.152

[48] M.A.Al Ibrahim, A. Kerimov, T. Mukerji, G. Mavko. Particula: A simulator tool for computational rock physics of granular media. Geophysics, 2019, 84: F85-F95. https://doi.org/10.1190/geo2018-0481.1

[49] B. Lin, Y. Shi, N. Cai. Numerical simulation of cell-to-cell performance variation within a syngas-fuelled planar solid oxide fuel cell stack. Applied Thermal Engineering, 2017, 114: 653-662. https://doi.org/10.1016/j.applthermaleng.2016.12.014

[50] Y. Wang, Y. Du, M. Ni, R. Zhan, Q. Du, K. Jiao. Three-dimensional modeling of flow field optimization for co-electrolysis solid oxide electrolysis cell. Applied Thermal Engineering, 2020, 172: 114959. https://doi.org/10.1016/j.applthermaleng.2020.114959

[51] Y. Shi, N. Cai, C. Li, C. Bao, E. Croiset, J. Qian, Q. Hu, S. Wang. Modeling of an anode-supported Ni–YSZ| Ni–ScSZ| ScSZ| LSM–ScSZ multiple layers SOFC cell: Part I.

experiments, model development and validation. Journal of Power Sources, 2007, 172(1): 235-245. https://doi.org/10.1016/j.jpowsour.2007.04.037

[52] C. Bao, Y. Wang, D. Feng, Z. Jiang, X. Zhang. Macroscopic modeling of solid oxide fuel cell (SOFC) and model-based control of SOFC and gas turbine hybrid system. Progress in Energy and Combustion Science, 2018, 66: 83-140. https://doi.org/10.1016/j.pecs.2017.12.002

[53] J. Hong, A. Bhardwaj, Y. Namgung, H. Bae, S. J. Song. Evaluation of the effects of nanocatalyst infiltration on the SOFC performance and electrode reaction kinetics using the transmission line model. Journal of Materials Chemistry A, 2020, 8(44): 23473-23487. https://doi.org/10.1039/D0TA07166H

[54] B. Mo, J. Rix, U. Pal, S. Basu, S. Gopalan. Improving SOFC Anode Electrocatalytic Activity Using Nanoparticle Infiltration into MIEC Compositions. Journal of The Electrochemical Society, 2020, 167(13): 134506. https://doi.org/10.1149/1945-7111/abb70f

[55] B. Molero-Sánchez, P. Addo, A. Buyukaksoy, V. Birss. Performance Enhancement of La0. 3Ca0. 7Fe0. 7Cr0. 3O3-δ Air Electrodes by Infiltration Methods. Journal of The Electrochemical Society, 2017, 164(10): F3123. https://doi.org/10.1149/2.0151710jes

Figure

(1) **Figure 1** Computation domain

(2) **Figure 2** (a) D3Q7 Lattice Boltzmann method; (b) Schematic diagram of computational procedure

(3) **Figure 3** Experimental comparison of KMC method. (a)Relative density evolution during sintering process; (b) Surface area & Relative density. Experimental comparison of LB method between different working conditions (Porosity: 0.44; Surface area:5.65 μm^2 μm^{-3}). (c) 20%, 50% O_2 mole fraction at 1023 K; (d) Temperature 973 K, 1023 K, 1073 K with 20% O_2 mole fraction

(4) **Figure 4** Influence of O_2 local partial pressure on electrode overpotential, 1023 K, I=1500 A m^{-2}. (a) Ohmic overpotential; (b) Active overpotential.

(5) **Figure 5** O2 concentration, ionic and electronic overpotential distribution of LSCF electrode, 1023 K, O_2 50%, I=1500 A m^{-2}

(6) **Figure 6** Effects of initial grainsize (0.2μm, 0.3μm and 0.4μm) on electrode performance, 1023 K, O_2 50%, I=1500 A m^{-2}; (a) Activation overpotential distribution; (b) Reaction rate distribution

(7) **Figure 7** Influence of compact powder uniformity, 1023 K, O_2 50%, I=1500 A m-2. (a) Activation overpotential distribution; (b) Comparison of activation polarization distribution; (c) Comparison of reaction rates distribution.

(8) **Figure 8** Performance comparison between regular and irregular compact powder, 1023 K, O_2 50%, I=1500 A m^{-2}. (a) Sintering precursor; (b) Activation overpotential distribution; (c) Reaction rates distribution;

(9) **Figure 9** Effects of sintering time on electrode performance, 1023 K, O_2 50%, I=1500 A m^{-2}. (a) Ohmic loss; (b) Activation loss; (c) Reaction rates distribution;

(10) **Figure 10** Performance comparison of traditional electrode and infiltrated electrode, 1023 K, O_2 50%, I=1500 A m^{-2}. (a) activation overpotential distribution; (b) Average reaction rates distribution along x direction, 1 active site=25×10^{-18} m^2;

(11) **Figure 11** Influence of nanoparticle size on electrode performance, 1023 K, O_2 50%, I=1500 A m^{-2}. (a) activation overpotential distribution; (b) Average reaction rates distribution along x direction, 1 active site=25×10^{-18} m^2;

(12) **Figure 12** Influence of infiltration load on electrode performance, 1023 K, O_2 50%, I=1500 A m^{-2}. (a) activation overpotential distribution; (b) Average reaction rates distribution along x direction, 1 active site=25×10^{-18} m^2;

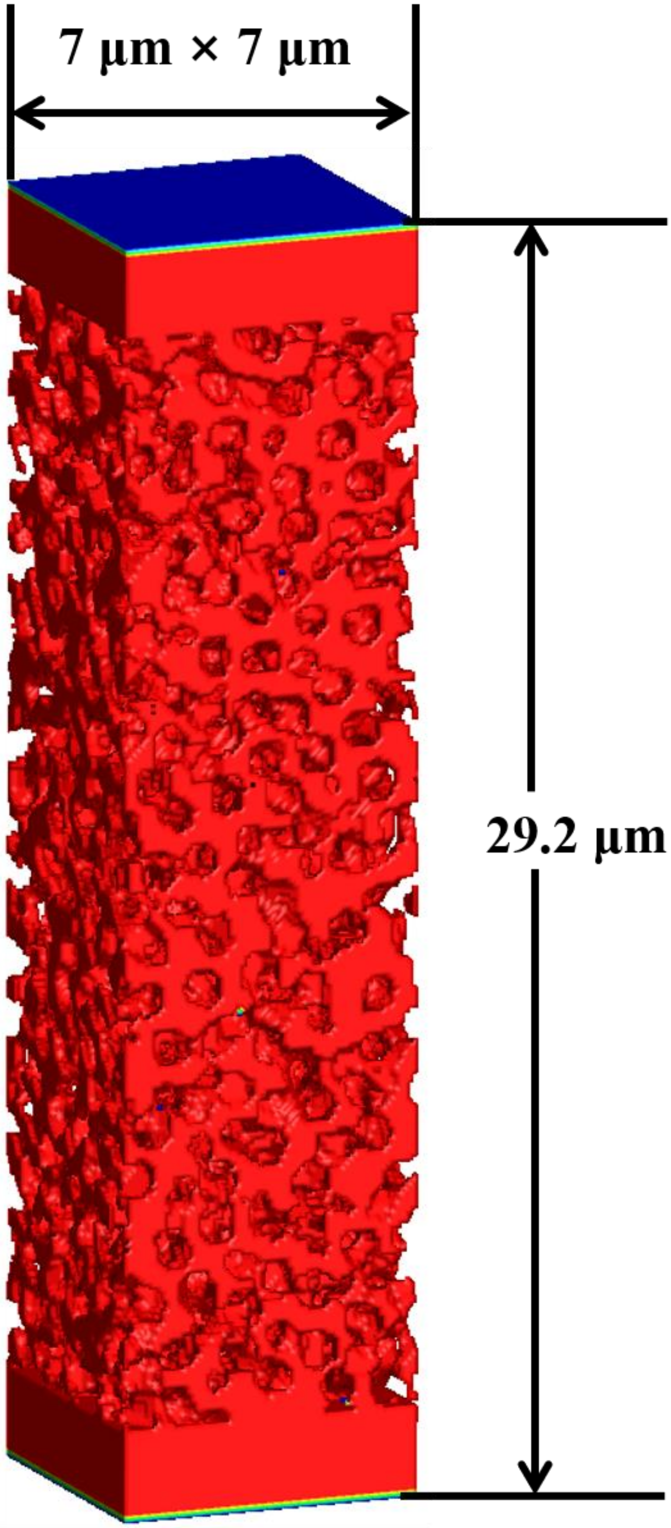

Figure 1 Computation domain

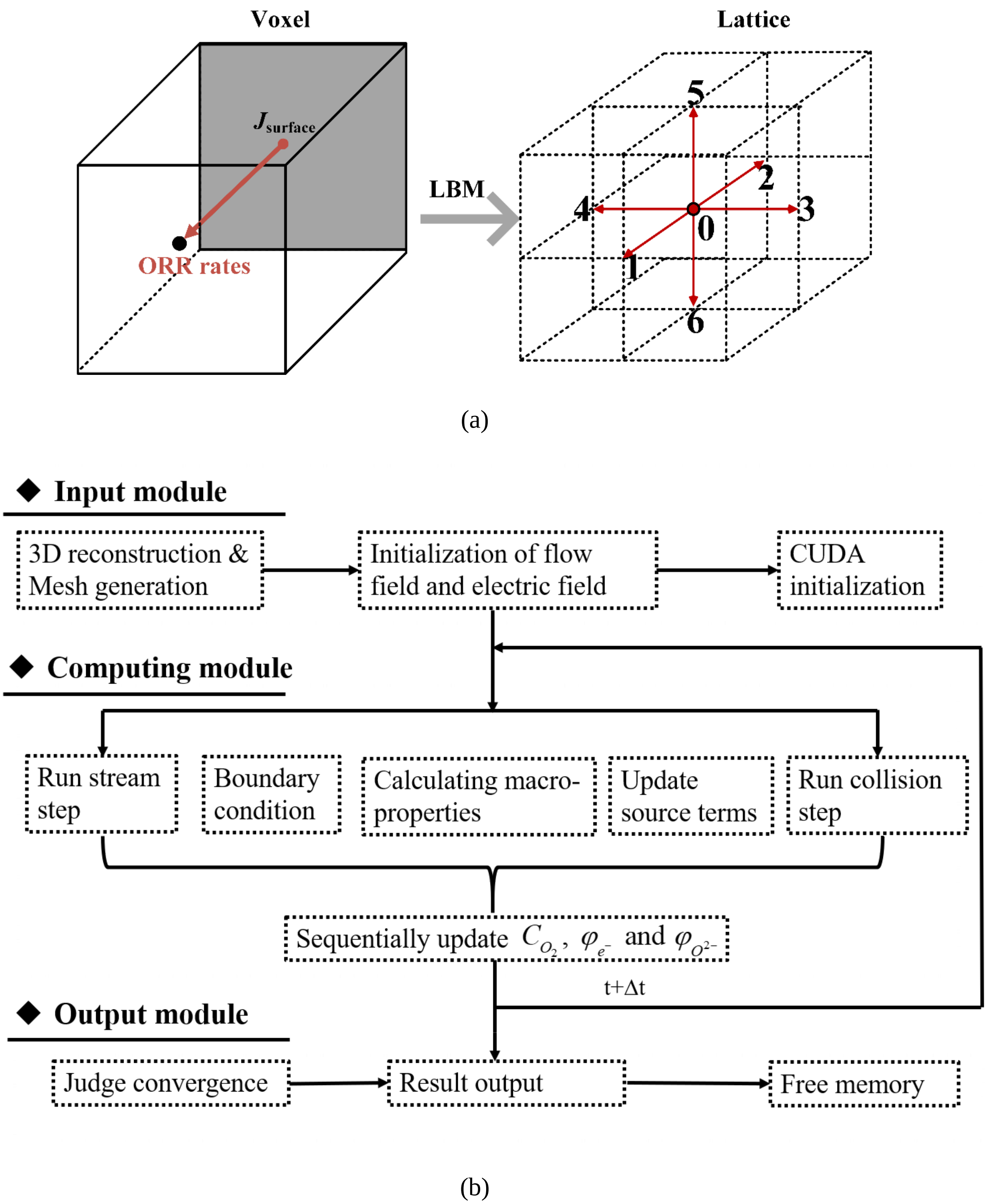

(a)

(b)

Figure 2 (a) D3Q7 Lattice Boltzmann method; (b) Schematic diagram of computational procedure

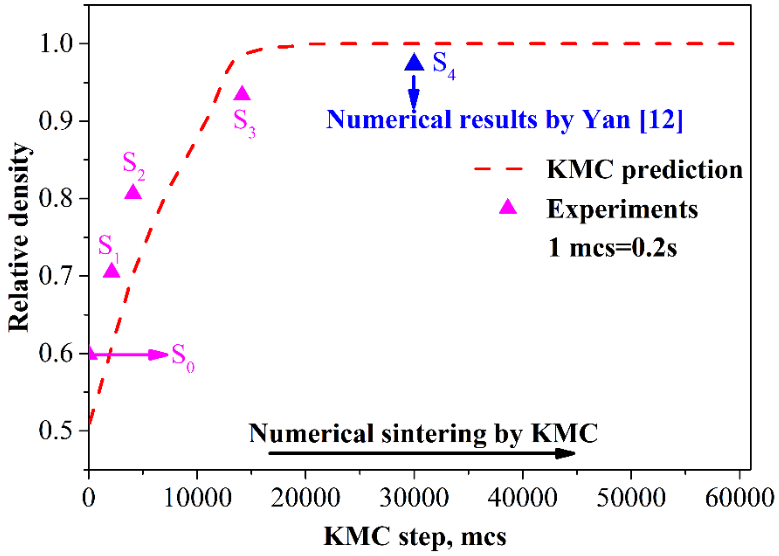
1.0
0.9
0.8
0.7
0.6
0.5
Relative density
0
10000
20000
30000
40000
50000
60000
KMC step, mcs
S_4
Numerical results by Yan [12]
S_3
S_2
S_1
S_0
KMC prediction
Experiments
1 mcs=0.2s
Numerical sintering by KMC

(a)

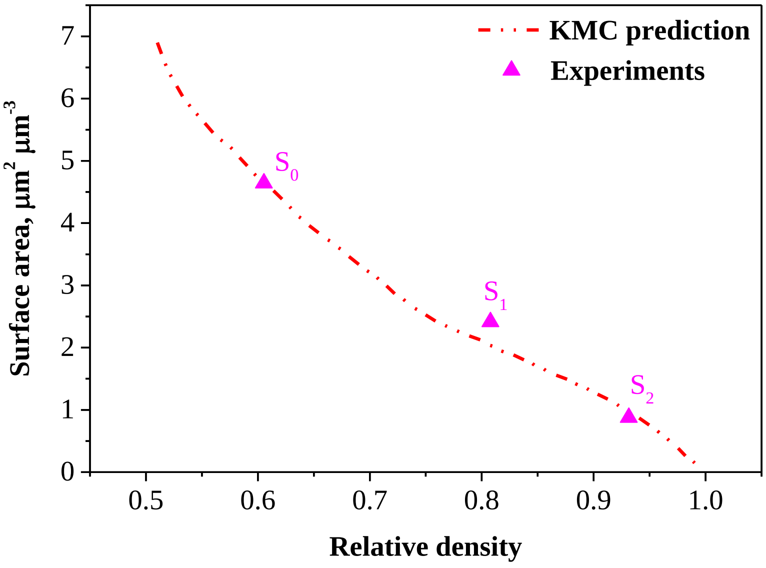
7
6
5
4
3
2
1
0
Surface area, μm^2 μm^{-3}
0.5
0.6
0.7
0.8
0.9
1.0
Relative density
KMC prediction
Experiments
S_0
S_1
S_2

(b)

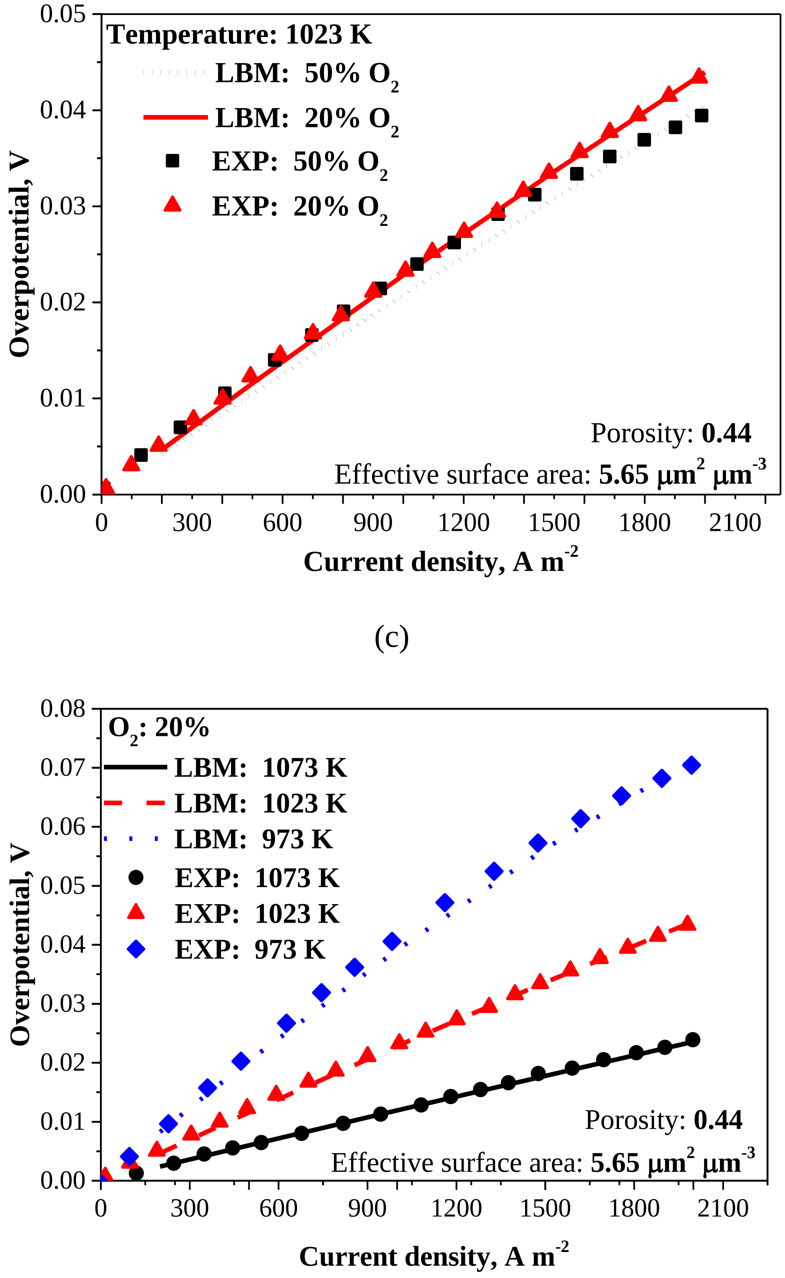

Figure 3 Experimental validation of KMC method. (a) Relative density evolution during sintering process; (b) Surface area & Relative density. Experimental comparison of LB method under different working conditions (Porosity: 0.44; Surface area:5.65 μm^2 μm^{-3}). (c) 20%, 50% O_2 mole fraction at 1023 K; (d) Temperature 973 K, 1023 K, 1073 K with 20% O_2 mole fraction.

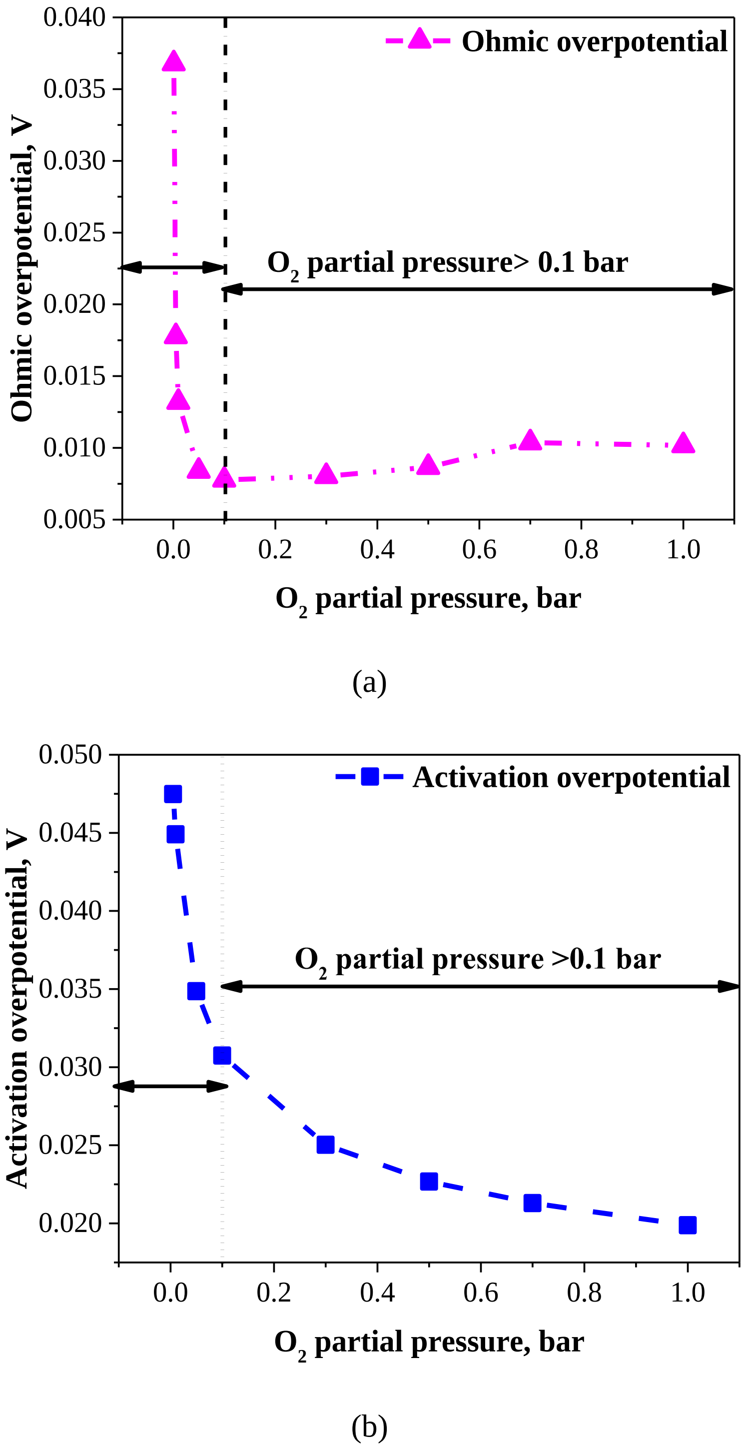

(a)

(b)

Figure 4 Influence of O_2 local partial pressure on electrode overpotential, 1023 K, I=1500 A m^{-2}. (a) Ohmic overpotential; (b) Active overpotential.

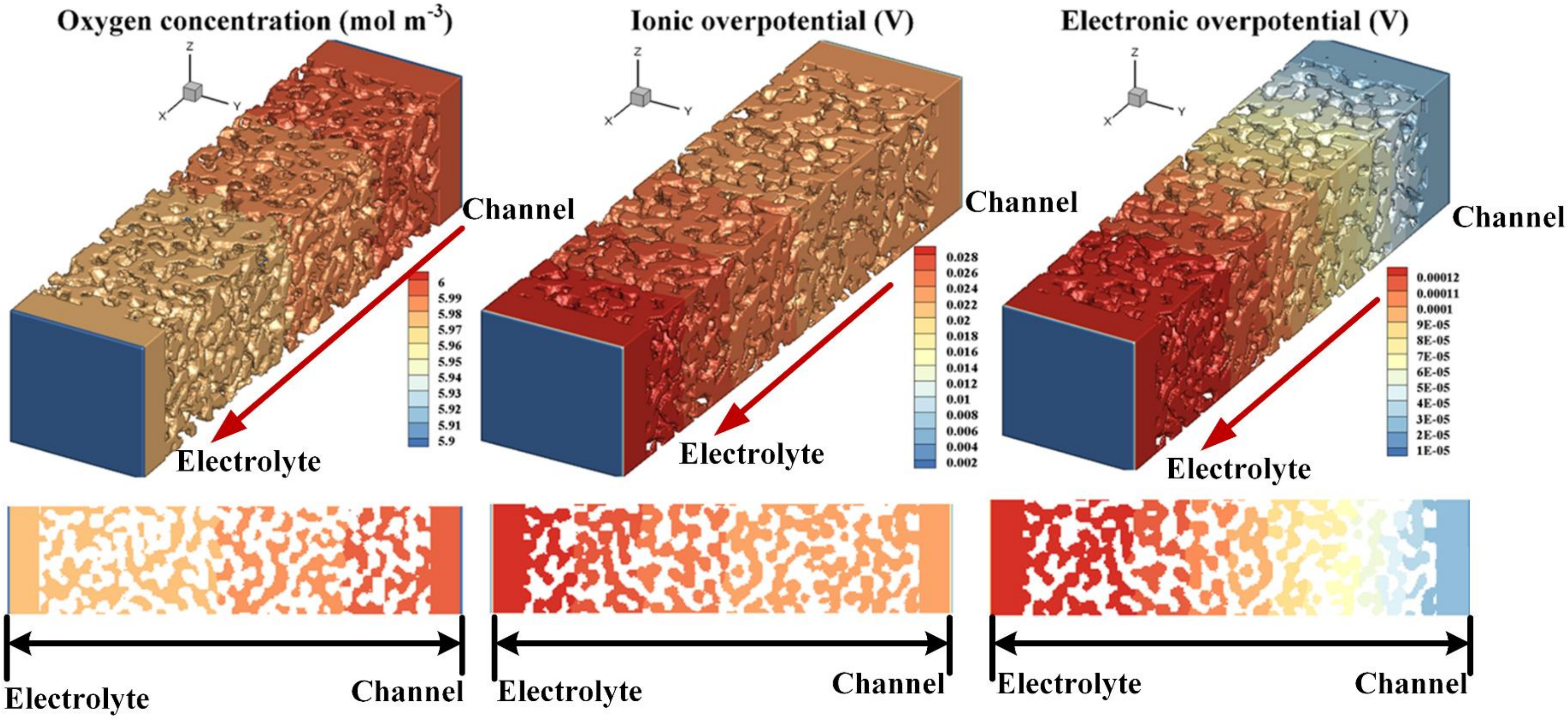

Figure 5 O_2 concentration, ionic and electronic overpotential distribution of LSCF electrode, 1023 K, O_2 50%, I=1500 A m^{-2}

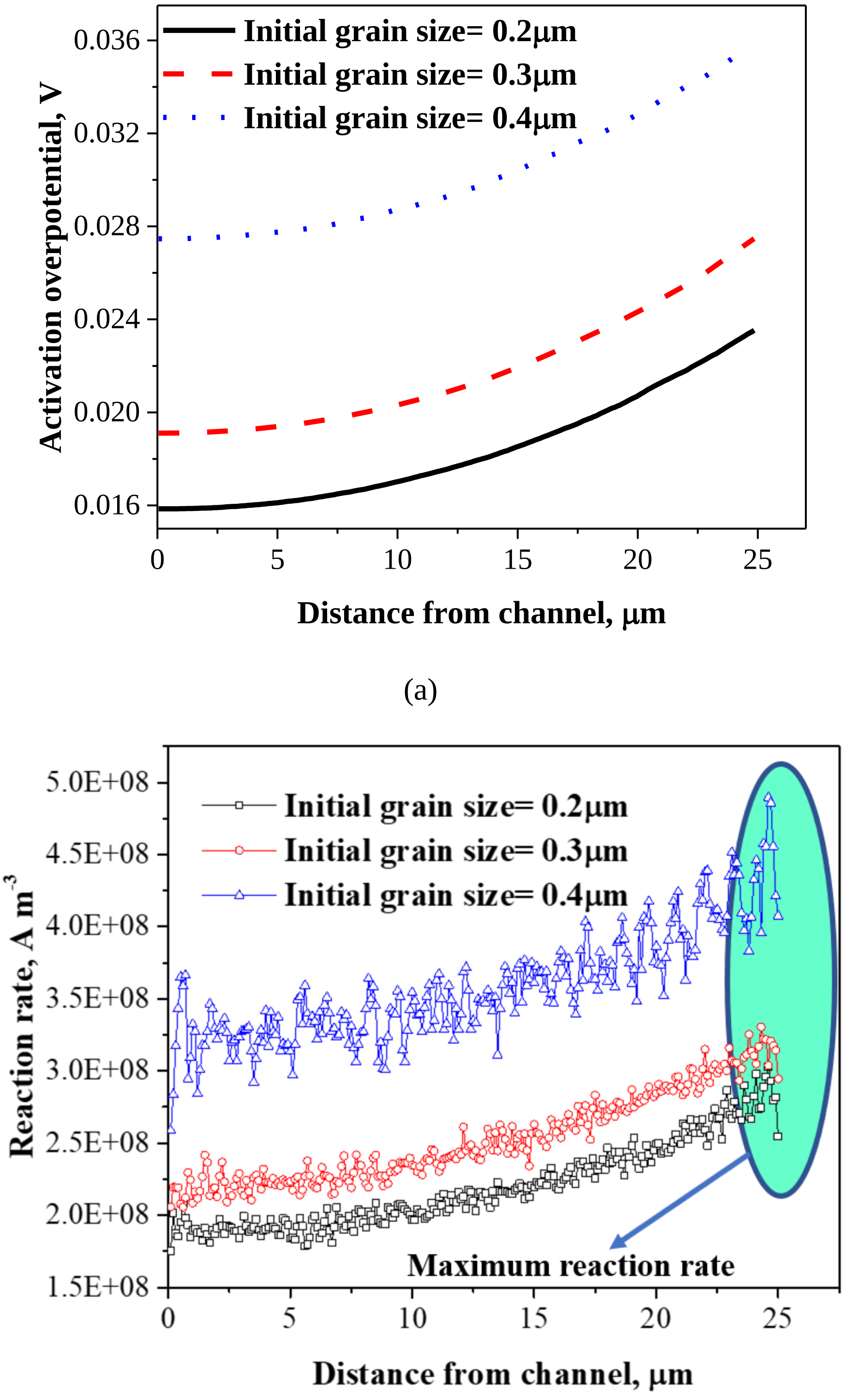

(a)

(b)

Figure 6 Effects of initial grainsize (0.2μm, 0.3μm and 0.4μm) on electrode performance, 1023 K, O_2 50%, I=1500 A m^{-2}; (a) Activation overpotential distribution; (b) Reaction rate distribution

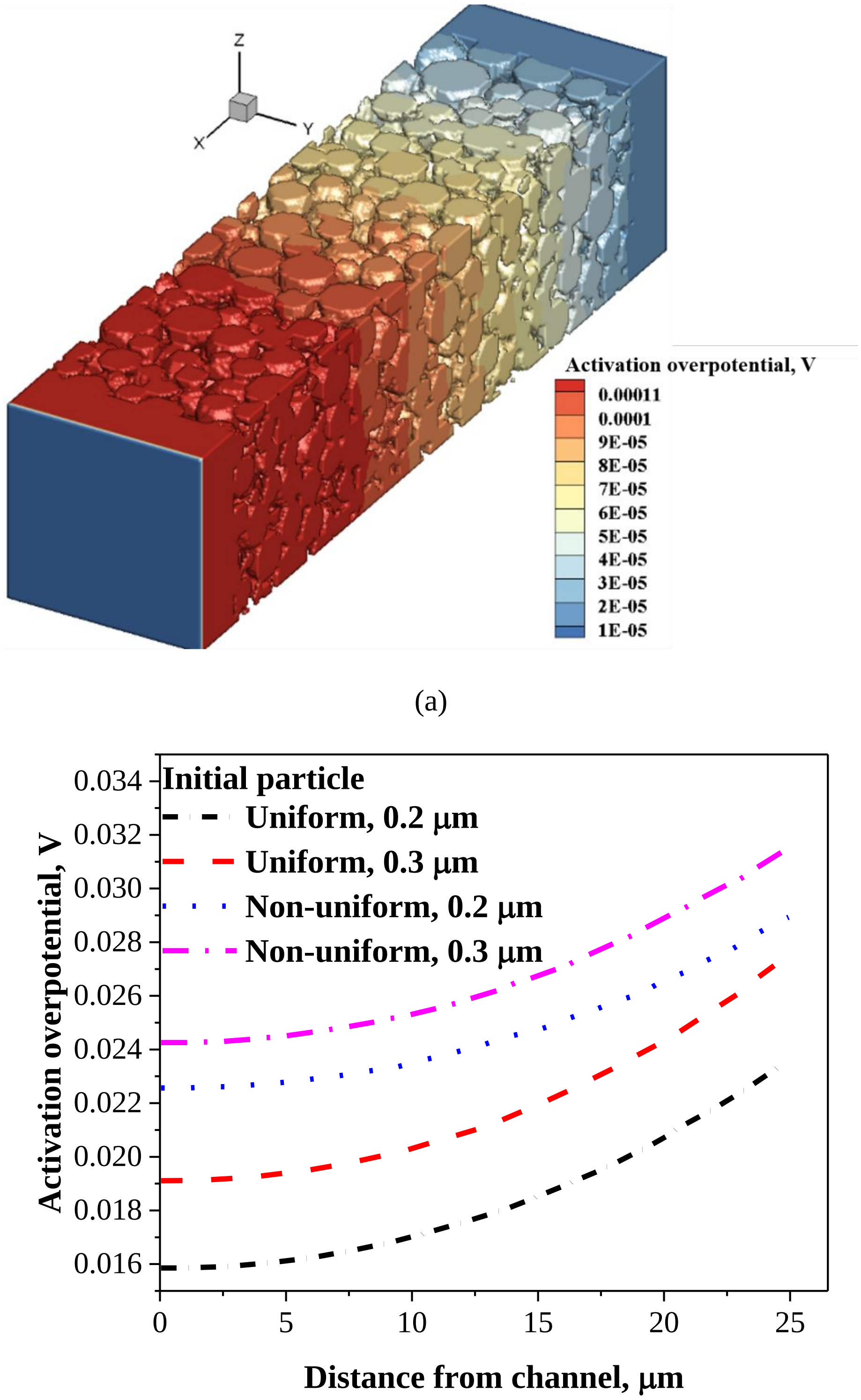
Z
X
Y
Activation overpotential, V
0.00011
0.0001
9E-05
8E-05
7E-05
6E-05
5E-05
4E-05
3E-05
2E-05
1E-05
Initial particle
Uniform, 0.2 μm
Uniform, 0.3 μm
Non-uniform, 0.2 μm
Non-uniform, 0.3 μm
Activation overpotential, V
0.034
0.032
0.030
0.028
0.026
0.024
0.022
0.020
0.018
0.016
0
5
10
15
20
25
Distance from channel, μm

(a)

(b)

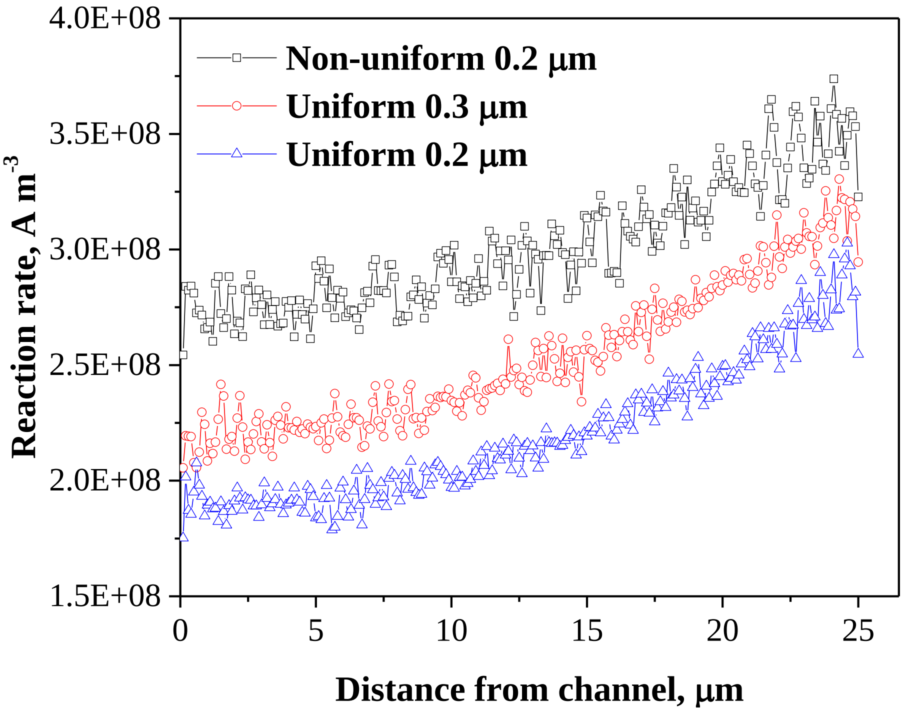

(c)

Figure 7 Influence of compact powder uniformity, 1023 K, O_2 50%, I=1500 A m^{-2}.

(a) Activation overpotential distribution; (b) Comparison of activation polarization distribution; (c) Comparison of reaction rates distribution.

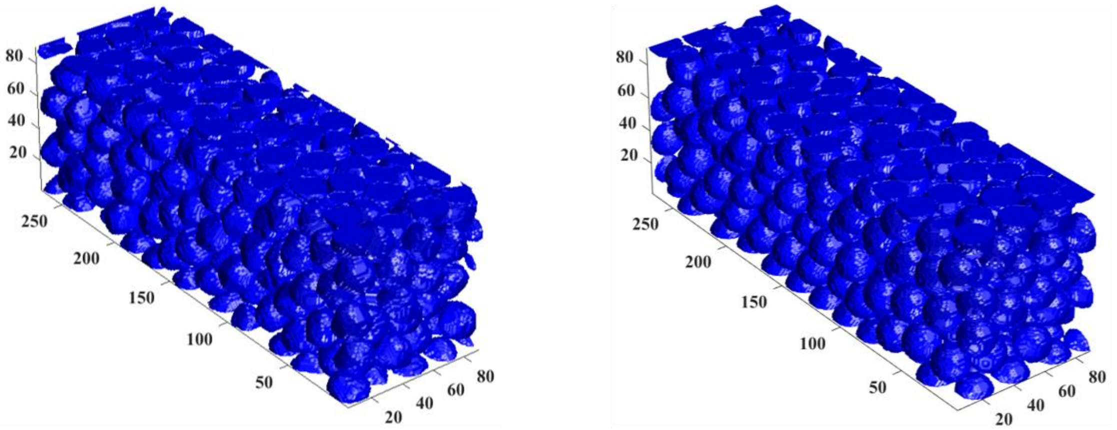

Irregular initial powder

Regular initial powder

(a)

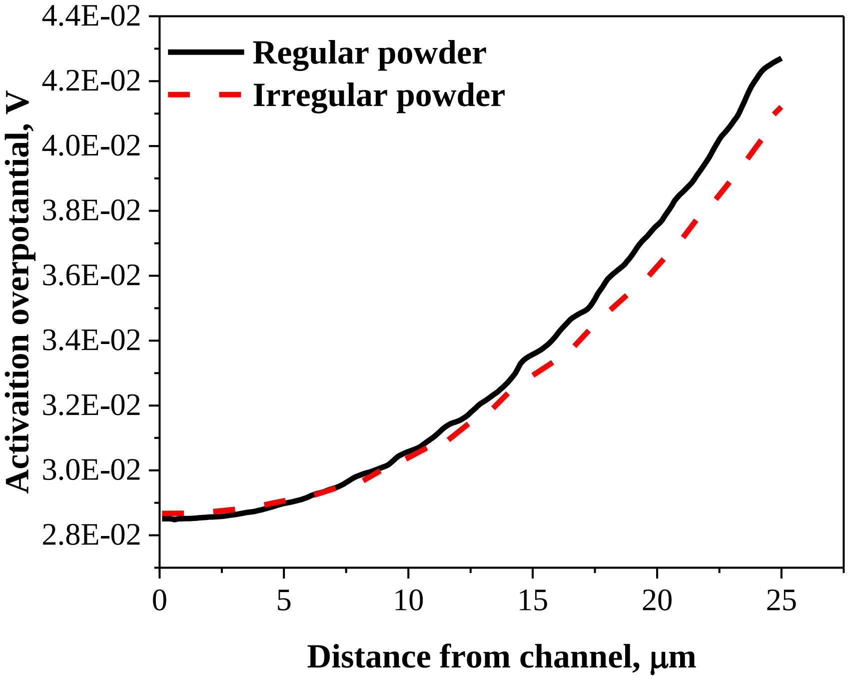

(b)

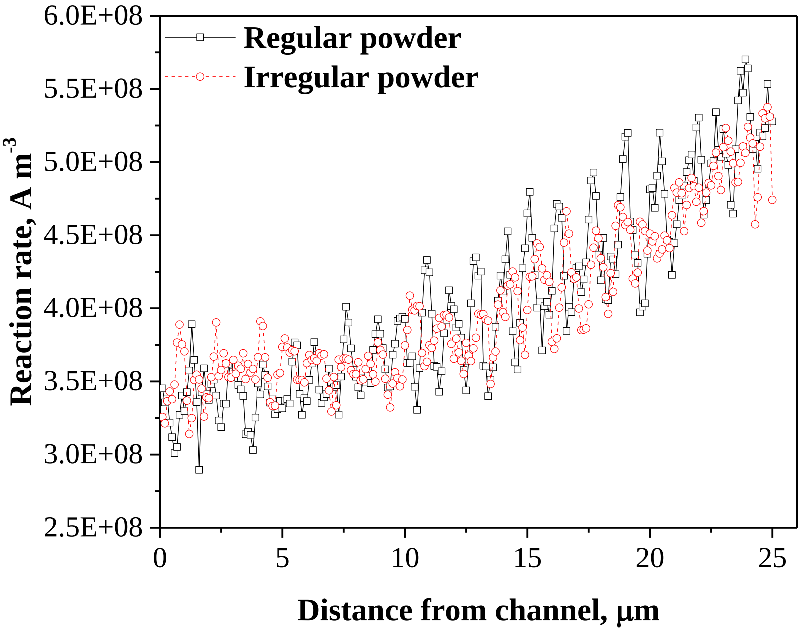

(c)

Figure 8 Performance comparison between regular and irregular compact powder, 1023 K, O_2 50%, I=1500 A m^{-2}. (a) Sintering precursor (resolution=100 nm); (b) Activation overpotential distribution; (c) Reaction rates distribution;

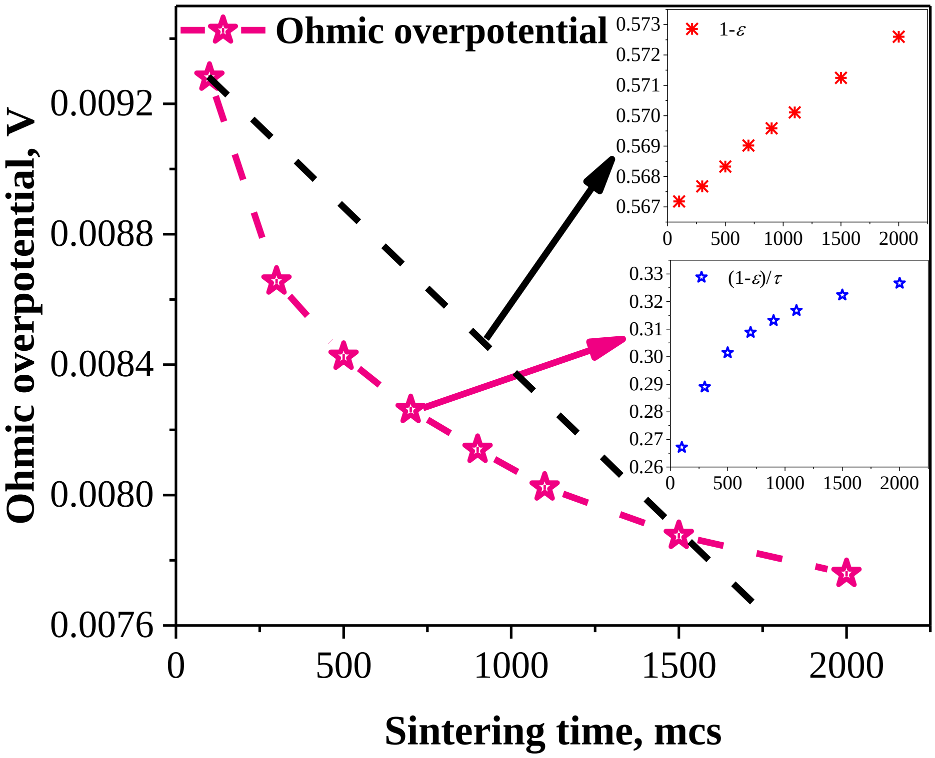
Ohmic overpotential
Ohmic overpotential, V
0.0092
0.0088
0.0084
0.0080
0.0076
0
500
1000
1500
2000
Sintering time, mcs
1-ε
0.573
0.572
0.571
0.570
0.569
0.568
0.567
0
500
1000
1500
2000
$(1-\varepsilon)/\tau$
0.33
0.32
0.31
0.30
0.29
0.28
0.27
0.26
0
500
1000
1500
2000

(a)

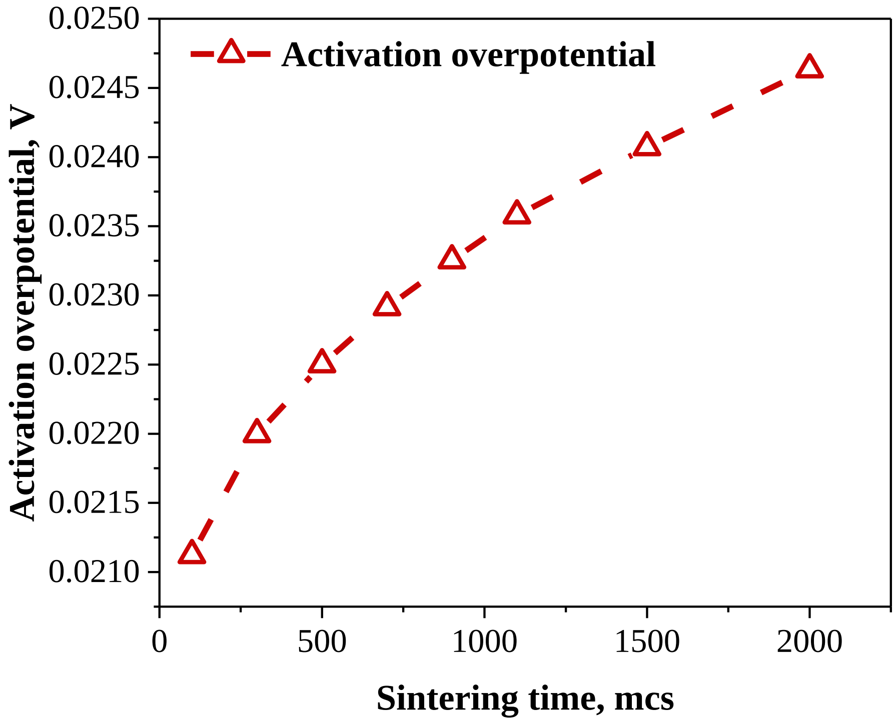
Activation overpotential
Activation overpotential, V
0.0250
0.0245
0.0240
0.0235
0.0230
0.0225
0.0220
0.0215
0.0210
0
500
1000
1500
2000
Sintering time, mcs

(b)

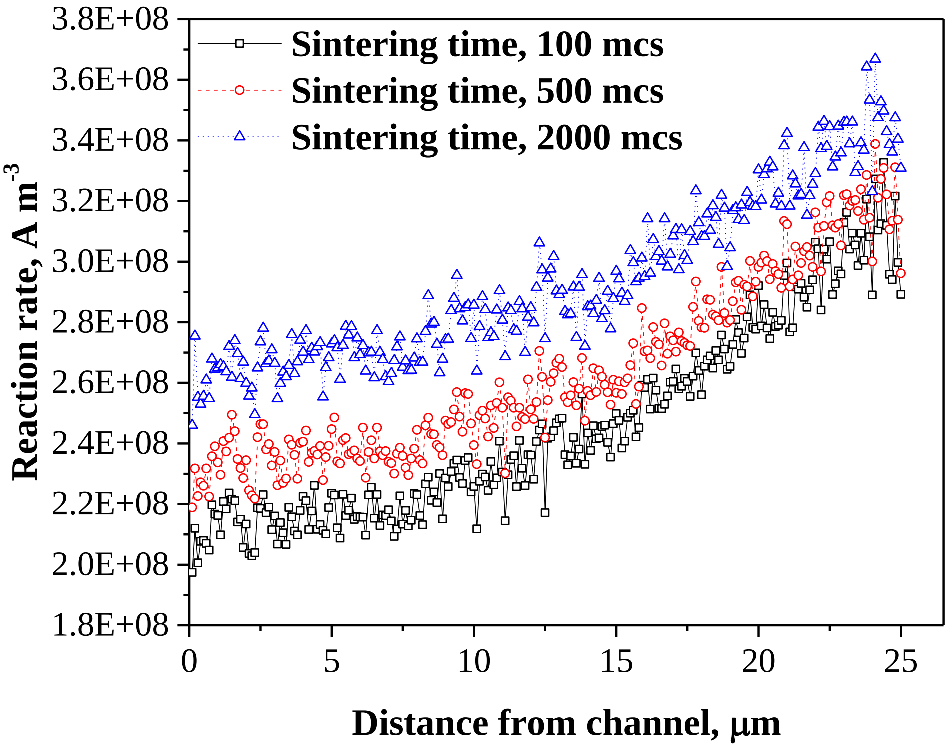

(c)

Figure 9 Effects of sintering time on electrode performance, 1023 K, O_2 50%, *I*=1500 A m^{-2}. (a) Ohmic loss; (b) Activation loss; (c) Reaction rates distribution;

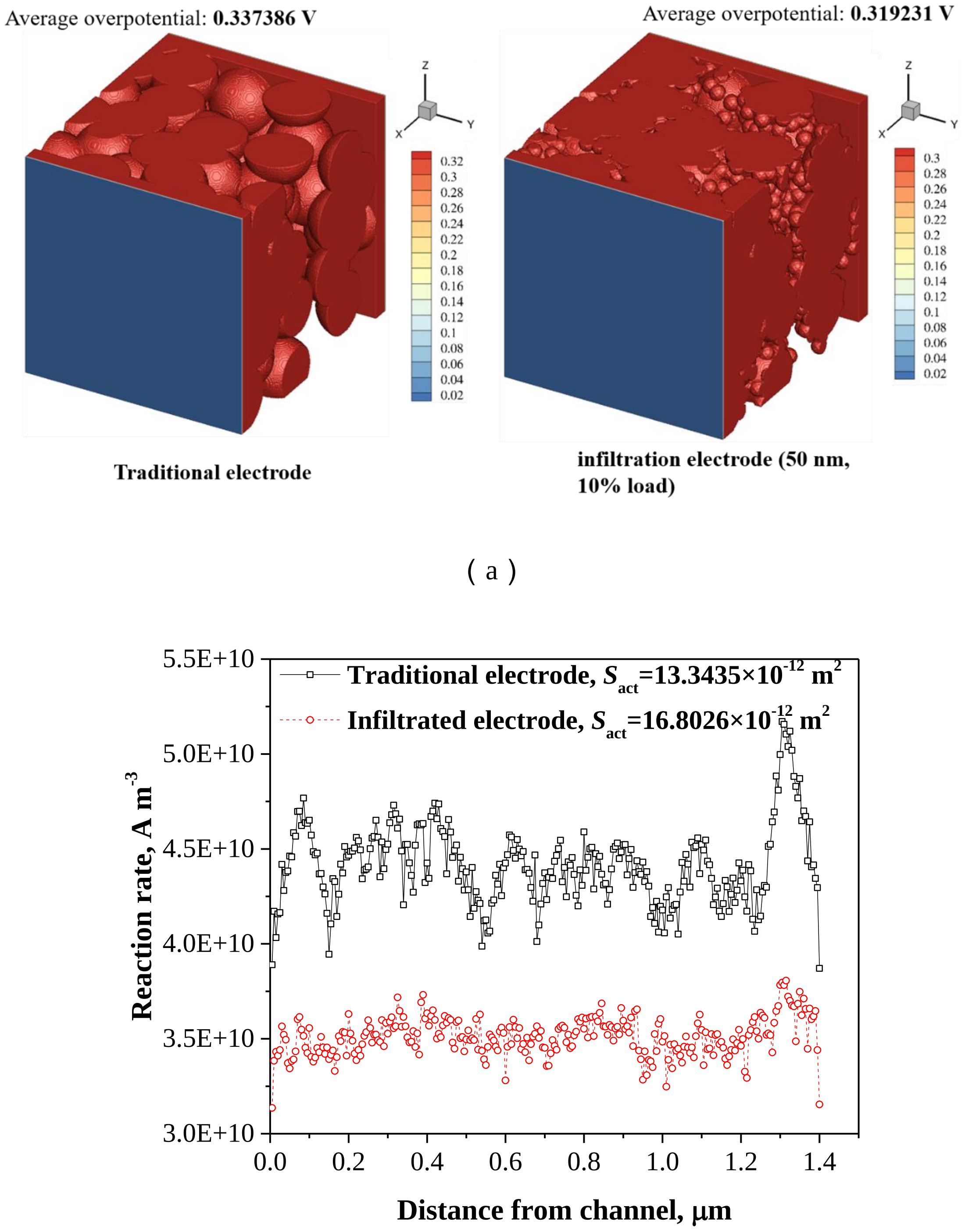

(a)

(b)

Figure 10 Performance comparison of traditional electrode and infiltrated electrode, 1023 K, O_2 50%, I=1500 A m^{-2}. (a) Activation overpotential distribution; (b) Average reaction rates distribution along x direction, 1 active site=25×10^{-18} m^2;

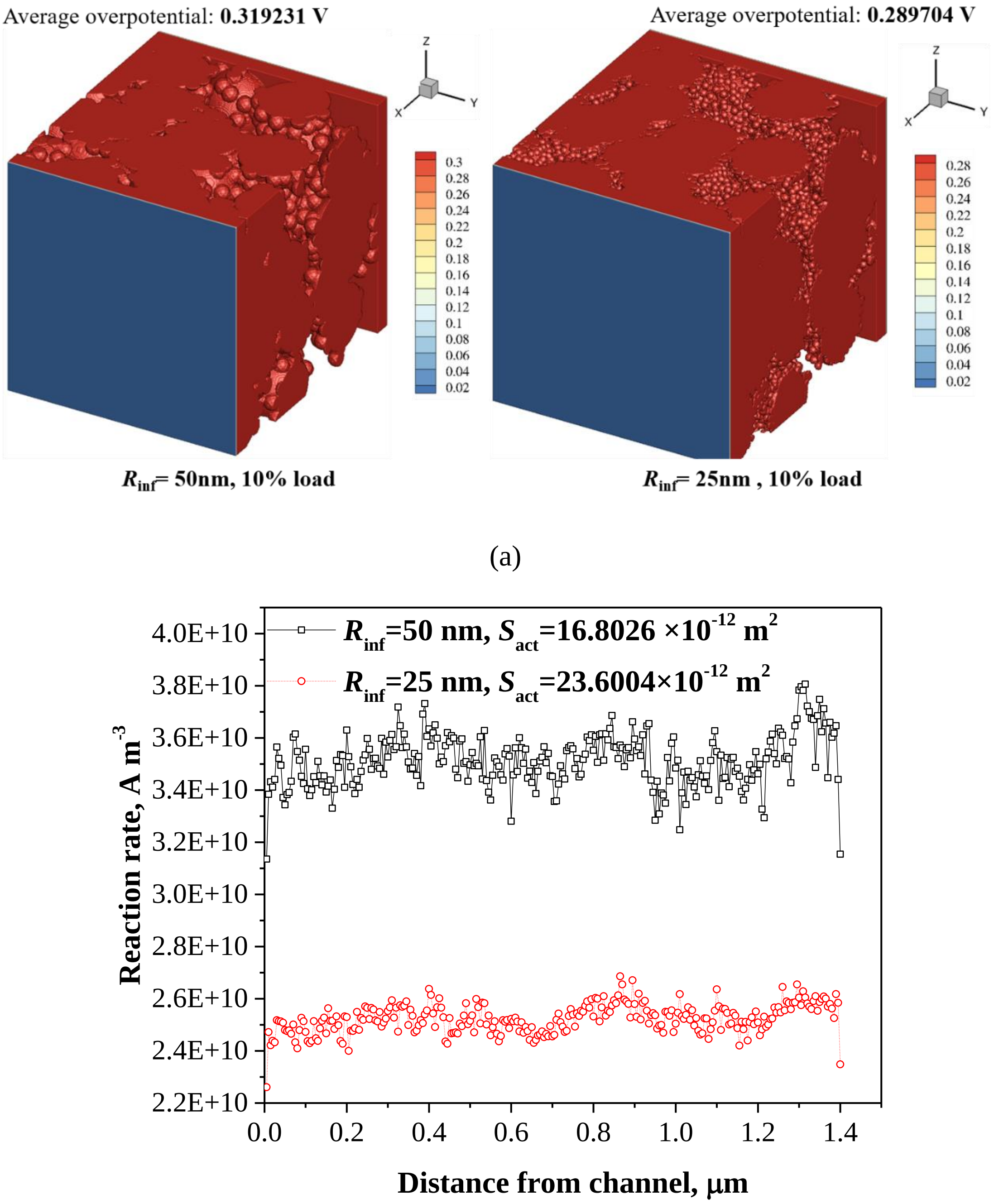

(a)

(b)

Figure 11 Influence of nanoparticle size on electrode performance, 1023 K, O_2 50%, I=1500 A m^{-2}. (a) Activation overpotential distribution; (b) Average reaction rates distribution along x direction, 1 active site=25×10^{-18} m^2;

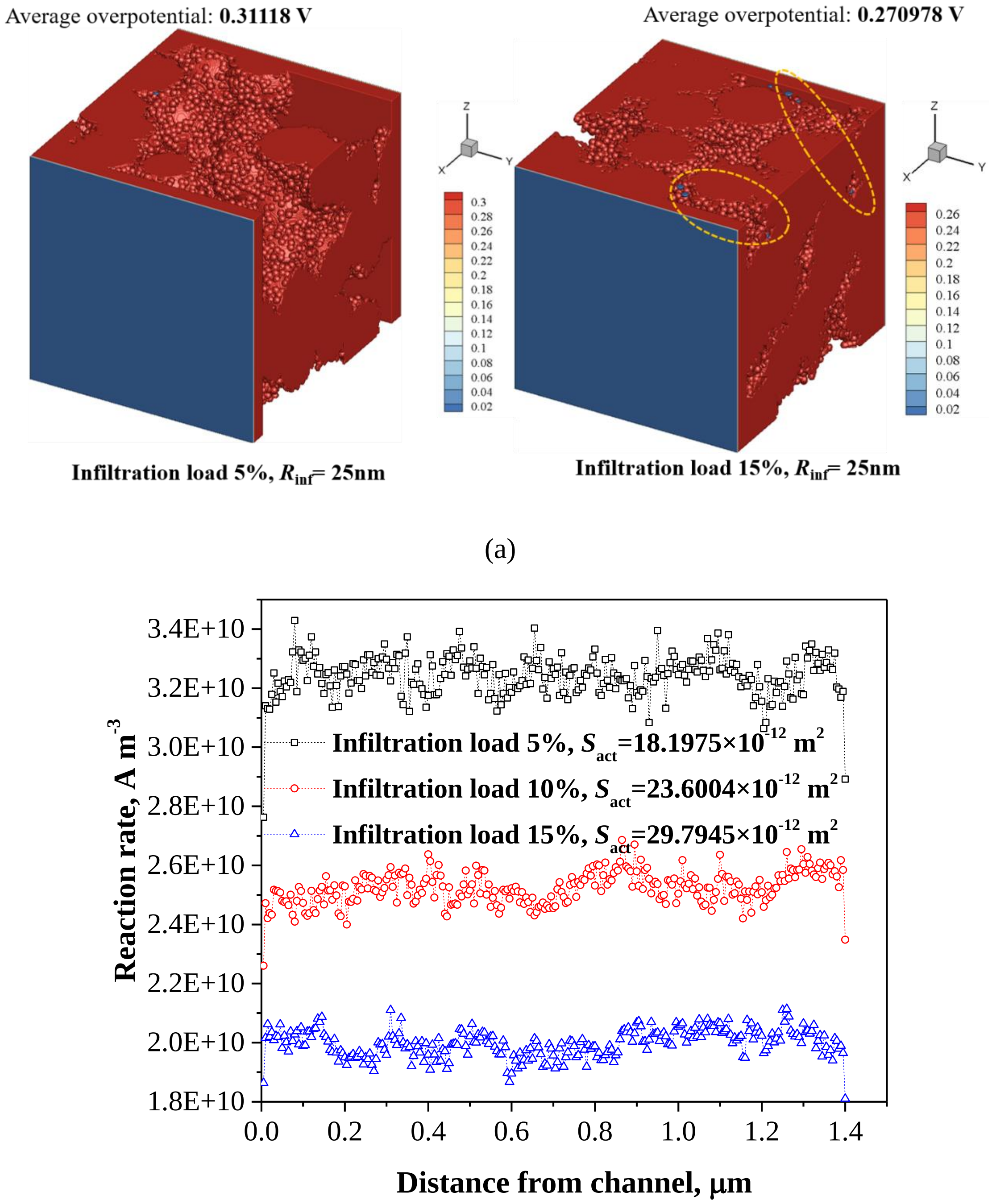

Figure 12 Influence of infiltration load on electrode performance, 1023 K, O_2 50%, I=1500 A m^{-2}. (a) Activation overpotential distribution; (b) Average reaction rates distribution along x direction, 1 active site=25×10^{-18} m^2;